

THE EXTENDED HALO OF CENTAURUS A: UNCOVERING SATELLITES, STREAMS AND SUBSTRUCTURES*

D. CRNOJEVIĆ¹, D. J. SAND¹, K. SPEKKENS², N. CALDWELL³, P. GUHATHAKURTA⁴, B. MCLEOD³, A. SETH⁵, J. D. SIMON⁶, J. STRADER⁷, E. TOLOBA^{1,4}

Draft version September 13, 2018

ABSTRACT

We present the widest-field resolved stellar map to date of the closest ($D \sim 3.8$ Mpc) massive elliptical galaxy NGC 5128 (Centaurus A; Cen A), extending out to a projected galactocentric radius of ~ 150 kpc. The dataset is part of our ongoing Panoramic Imaging Survey of Centaurus and Sculptor (PISCeS) utilizing the Magellan/Megacam imager. We resolve a population of old red giant branch stars down to ~ 1.5 mag below the tip of the red giant branch, reaching surface brightness limits as low as $\mu_{V,0} \sim 32$ mag arcsec⁻². The resulting spatial stellar density map highlights a plethora of previously unknown streams, shells, and satellites, including the first tidally disrupting dwarf around Cen A (CenA-MM-Dw3), which underline its active accretion history. We report 13 previously unknown dwarf satellite candidates, of which 9 are confirmed to be at the distance of Cen A (the remaining 4 are not resolved into stars), with magnitudes in the range $M_V = -7.2$ to -13.0 , central surface brightness values of $\mu_{V,0} = 25.4 - 26.9$ mag arcsec⁻², and half-light radii of $r_h = 0.22 - 2.92$ kpc. These values are in line with Local Group dwarfs but also lie at the faint/diffuse end of their distribution; interestingly, CenA-MM-Dw3 has similar properties to the recently discovered ultra-diffuse galaxies in Virgo and Coma. Most of the new dwarfs are fainter than the previously known Cen A satellites. The newly discovered dwarfs and halo substructures are discussed in light of their stellar populations, and they are compared to those discovered by the PAndAS survey of M31.

Subject headings: galaxies: groups: individual (CenA) — galaxies: halos — galaxies: dwarf — galaxies: photometry

1. INTRODUCTION

The currently favored Λ Cold Dark Matter (Λ CDM) cosmological scenario is successful at reproducing the observed properties of large-scale structures, but it encounters challenges at galactic scales, particularly at the low-luminosity end (e.g., Weinberg et al. 2013). The Λ CDM cosmology predicts a bottom-up hierarchical assembly of structures, with the smallest halos critically contributing to the build-up of the most massive ones. The number and physical properties of stellar streams associated with accreted halos are major predictions of Λ CDM (e.g., Bullock & Johnston 2005; Johnston et al. 2008; Cooper et al. 2010), and since dynamical timescales at large galactocentric distances are comparable to the age of the Universe, accretion events can be effectively caught in the act in the outskirts of galaxies.

Disrupting satellites and streams are clearly detected in the Milky Way (MW) and M31 (e.g.,

Ibata et al. 1994; Belokurov et al. 2006; Grillmair 2006, 2009; Bonaca et al. 2012; Grillmair et al. 2013; Bernard et al. 2014; Ibata et al. 2014; Koposov et al. 2014; Belokurov & Koposov 2016), but there are significant differences between them despite their shared environment and similar mass: the halo of M31 seems to present a substantially larger number of substructures than the MW (with the caveat that we might be missing some of the substructure of the MW due to our position within it), indicating an enhanced level of interaction and/or a more active and prolonged accretion history (Richardson et al. 2008; Deason et al. 2013; Pillepich et al. 2014; Dorman et al. 2015). The stochasticity of the hierarchical assembly process implies that a broad diversity of halo to halo substructure is expected at any given halo mass (e.g., Purcell et al. 2007) due to different accretion histories (e.g., Johnston et al. 2008; Busha et al. 2010), and the relative contributions of in-situ star formation and disrupted satellites remain poorly understood (e.g., Pillepich et al. 2014; Tissera & Scannapieco 2014; Lu et al. 2015). While we can study galaxies within the Local Group (LG) in the most detail due to their proximity, they may not be representative of generic MW-mass halos.

Streams/substructures are known to be a common feature in the halos of giant galaxies beyond the LG (Mouhcine et al. 2010; Atkinson et al. 2013; Martínez-Delgado et al. 2010; Duc et al. 2015), thus lending credence to Λ CDM models. However, their mere detection only provides a qualitative comparison set with simulations: more quantitative observational constraints from a wide range of galaxies are urgently needed to

* This paper includes data gathered with the 6.5 meter Magellan Telescopes located at Las Campanas Observatory, Chile.

¹ Department of Physics, Texas Tech University, Box 41051, Lubbock, TX 79409-1051, USA; denija.crnojevic@ttu.edu

² Department of Physics, Royal Military College of Canada, Box 17000, Station Forces, Kingston, Ontario K7L 7B4, Canada

³ Harvard-Smithsonian Center for Astrophysics, Cambridge, MA 02138, USA

⁴ UCO/Lick Observatory, University of California, Santa Cruz, 1156 High Street, Santa Cruz, CA 95064, USA

⁵ Department of Physics and Astronomy, University of Utah, Salt Lake City, UT 84112, USA

⁶ Observatories of the Carnegie Institution for Science, 813 Santa Barbara Street, Pasadena, CA 91101, USA

⁷ Department of Physics and Astronomy, Michigan State University, East Lansing, MI 48824, USA

verify predictions for the assembly of galaxy halos at a deeper level. Halos and their satellites and substructures in galaxies beyond the LG are extremely challenging to survey because of their intrinsic faintness. Integrated light studies suffer from degeneracies in age, metallicity and extinction and, despite being able to detect low surface brightness features and galaxies (e.g Atkinson et al. 2013; Merritt et al. 2014; Martínez-Delgado et al. 2010; Duc et al. 2015; Koda et al. 2015; Mihos et al. 2015; Müller et al. 2015; Muñoz et al. 2015), they cannot easily constrain distances. The direct imaging of individual stars is thus the ultimate way of revealing the information locked in outer halos. From their position in the color-magnitude diagram (CMD), it is possible to derive the stars’ physical properties, such as metallicity and/or age, with generally less severe degeneracies with respect to integrated studies, as well as accurate distances. *Hubble Space Telescope* (HST) imaging can make strategic contributions by drilling deep in selected, narrow fields (e.g., Dalcanton et al. 2009; Radburn-Smith et al. 2011; Rejkuba et al. 2005, 2014; Monachesi et al. 2016), but this strategy lacks the field of view to perform panoramic assessments of galaxy halos. Only wide-field imagers on ground-based telescopes can resolve stars over large areas for nearby ($D < 10$ Mpc) galaxies, but few such studies have been undertaken to date and they cover at most a few tens of kpc into the target halos (Mouhcine et al. 2010; Bailin et al. 2011; Barker et al. 2012; Greggio et al. 2014). A few pioneering works are however underway to survey larger portions of the spiral M81 (Chiboucas et al. 2009, 2013; Okamoto et al. 2015) and the dwarf spiral/irregular NGC 3109 (Sand et al. 2015).

At the same time, the discovery of an entirely new class of faint MW and M31 satellites ($M_V \gtrsim -8.0$) one decade ago has opened unexpected perspectives on galaxy formation at these low luminosities/masses (e.g., Willman et al. 2005; Belokurov et al. 2007; McConnachie et al. 2009; Martin et al. 2013), and continues to keep astronomers engaged with the most recent Dark Energy Survey (DES) and Panoramic Survey Telescope and Rapid Response System (Pan-STARRS) discoveries (e.g., Bechtol et al. 2015; Drlica-Wagner et al. 2015; Kim et al. 2015; Kim & Jerjen 2015; Kuposov et al. 2015; Laevens et al. 2015a,b; Martin et al. 2015). Despite our increasing knowledge of these lowest-mass systems, the infamous “missing satellite” and “too big to fail” problems (e.g., Moore et al. 1999; Boylan-Kolchin et al. 2011) are still calling for a definitive solution. The former problem, i.e., the overprediction of the number of dark matter subhalos around a MW halo in simulations compared to the observed numbers, can be effectively tackled by extending the census of low-mass satellites in environments beyond the LG.

We have addressed these challenges by starting an ambitious wide-field observational campaign (Panoramic Imaging Survey of Centaurus and Sculptor, or PISCeS) to search for faint satellites and signs of hierarchical structure formation in the halos of two nearby galaxies of different morphologies, the spiral NGC 253 ($D \sim 3.5$ Mpc; Radburn-Smith et al. 2011) and the elliptical NGC 5128, or Centaurus A (Cen A, $D \sim 3.8$ Mpc; Harris et al. 2010). The former (similar in mass to the

MW; Karachentsev 2005) is the dominant galaxy in the loose, elongated Sculptor group, while the latter (slightly more massive than the MW; Woodley et al. 2007) resides in a rich, more dynamically evolved group and shows signs of a recent gas-rich accretion event, thus we are probing opposite types of environment. Our project aims at resolving the extended halos of these galaxies out to projected radii (~ 150 kpc) similar to those reached by the Pan-Andromeda Archaeological Survey (PANdAS, see McConnachie et al. 2009; Ibata et al. 2014) and the Spectroscopic and Photometric Landscape of Andromeda’s Stellar Halo (SPLASH; Guhathakurta et al. 2005, 2006; Gilbert et al. 2012) around M31. PISCeS will complement and extend similar deep halo work in other nearby galaxy systems, sampling a range of morphologies and environments, with the goal of obtaining quantitative constraints on theoretical predictions. The PISCeS discoveries of two faint satellites around each of NGC 253 and Cen A are already reported in Crnojević et al. (2014b), Sand et al. (2014) and Toloba et al. (2016).

This paper presents the first general overview of the PISCeS survey for Cen A, within the coverage obtained to date ($\sim 70\%$ of the total planned area). In §2 we describe our survey and the data reduction process, while in §3 we present the global properties of the stellar populations and spatial stellar density map of the halo of Cen A. In §4 we focus on the new streams and substructures in the halo of Cen A and on their distances, as well as on the properties (surface brightness profile, structural parameters, luminosity) of its most robust newly discovered satellites, i.e., those confirmed to be at the distance of Cen A. In §5 we discuss the current results and the future contributions stemming from the PISCeS survey, which will include an investigation of the halo of Cen A profile, a detailed analysis of its satellites’ stellar populations, and the derivation of the satellite luminosity function of Cen A in light of our detection limits.

2. THE PISCES SURVEY

The outer halo of Cen A has been targeted as part of the PISCeS survey with the Megacam imager (McLeod et al. 2015) on the Magellan Clay 6.5-m telescope, Las Campanas Observatory. Megacam has a $\sim 24' \times 24'$ field-of-view and a binned pixel scale of $0''.16$. Over the course of 25 nights during the first semesters of 2010, 2011, 2013, 2014 and 2015, we have observed 80 fields around Cen A, out of which 5 had to be completely discarded due to poor observing conditions. The survey to date covers ~ 11 deg² and reaches out to a projected radius of ~ 150 kpc in the North and East direction and ~ 100 kpc in the South and West direction, with an additional extension along the North-West minor axis of Cen A out to ~ 200 kpc. The final year of observations is planned to be 2016, when we will reach the complete survey area of ~ 15 deg² by targeting the regions South and South-West of Cen A out to ~ 150 kpc.

A typical pointing taken in good seeing conditions is observed for 6×300 sec in both g - and r -band, except for a few cases where fewer individual exposures per filter were taken. The median seeing throughout the survey to date has been $\sim 0''.65$, the best/worst seeing being $\sim 0''.5/1''.3$ in both bands. In poorer seeing conditions ($\gtrsim 0''.9$) or in the presence of clouds, we increase

the exposure time by up to a factor of two. The exposure times and seeing conditions for each pointing will be fully reported in a future contribution, together with the final photometric catalogues. The individual exposures have been dithered in order to fill in the gaps between the 36 Megacam CCDs. The reduction process is performed by the Smithsonian Astrophysical Observatory Telescope Data Center, using a dedicated code developed by M. Conroy, J. Roll and B. McLeod, and details can be found in McLeod et al. (2015). Briefly, after standard pre-processing steps (overscan, bias, dark correction, flat-fielding, cosmic ray rejection, defringing, illumination correction, astrometric solution), the individual exposures are regridded and combined into stacks using SWARP (Bertin 2010).

We perform point spread function (PSF)-fitting photometry on each of the stacked final images (rather than on the individual exposures), using the suite of programs DAOPHOT and ALLFRAME (Stetson 1987, 1994). To construct a reliable PSF model, we pick $\sim 300 - 400$ isolated, non-saturated bright stars across the Megacam field-of-view and allow the model solution to vary as a function of position. The typical variation of the PSF across the field-of-view is on the order of $\sim 5\% - 10\%$. We set our source detection limit to 3σ above the background level, and derive photometry for each band with ALLSTAR. The catalogues for each band are matched with DAOMATCH/DAOMASTER (Stetson 1993), and then a final round of photometry is performed simultaneously in both bands through ALLFRAME, in order to increase photometric depth. Given the wide range of observing conditions, the quality cuts applied to the photometric catalogues are tailored to each pointing, and fluctuate around sharpness values of $|sharp| < 3$ and around $\chi < 1.5$. These cuts eliminate most contaminant galaxies.

Once the clean photometric catalogues are obtained for each pointing, we proceed to calibrate the instrumental magnitudes to the Sloan Digital Sky Survey (SDSS) system. Overlaps between adjacent pointings are part of our observing strategy, and are used to calibrate those pointings acquired under non-photometric conditions. Out of the 25 nights of observations, 8 were photometric: during each of these nights we observed two to three equatorial SDSS fields at different airmasses. We linearly derive zeropoints and color terms and their relative airmass dependence, and apply the calibration to all the pointings taken on that photometric night. For the remainder of the pointings, we propagate the calibration based on the overlapping regions, which are ~ 2 arcmin wide. We derive pointing-to-pointing zeropoints and color terms from these overlaps, using on average $\sim 100 - 300$ reference bright stars with calibrated magnitudes in the range $19 < r < 22$ and with photometric errors smaller than 0.05 mag. We ultimately compare pointings at opposite sides of the surveyed area in order to check our calibration: the overall median calibration uncertainty is estimated to be ~ 0.03 mag for each band across the entire survey. We finally trim the overlapping edges for adjacent pointings, keeping the photometry from the deepest one within each considered pair.

The final calibrated catalogues are dereddened on a source-by-source basis by interpolating the Schlegel et al. (1998) extinction maps and the Schlafly & Finkbeiner

(2011) correction coefficients: $A_g = 3.303 \times E(B - V)$ and $A_r = 2.285 \times E(B - V)$. The median reddening over the surveyed area is $E(B - V) \sim 0.12$, with spatial variations of up to $\sim 15\%$. For the rest of the paper we will be assuming dereddened g_0 and r_0 magnitudes. In Fig. 1, we present the global CMD of Cen A, which we discuss in further detail in Sect. 3.

2.1. Artificial star experiments

Given the varying observing conditions, the photometric depth is not uniform across the survey area (see also next section). It is thus critical to assess the photometric uncertainties and incompleteness to meaningfully interpret our wide-field dataset. For each pointing, we inject a number of fake stars between 5 and 10 times the number of recovered bona-fide sources (i.e., after applying the quality cuts to the photometric catalogues), distributed into tens of experiments in order not to increase stellar crowding artificially. The minimum number of fake stars produced is $\sim 10^6$ per pointing, and they are homogeneously distributed across the field-of-view of the pointing. The fake stars have a similar color-magnitude distribution to that of the observed sources, except for a deeper extension at faint magnitudes (down to ~ 2 mag fainter than the faintest real recovered stars), so as to take into account those faint objects that are upscattered in the observed CMD due to noise. Their photometry is derived exactly in the same way as for the real data, and the same quality cuts and calibration are applied.

The overall photometric incompleteness is a product of observing conditions (seeing and transparency), local stellar crowding, and spatial coverage (e.g., holes in the stellar distribution are often present due to saturated foreground stars). The color-averaged 50% completeness limit per pointing varies from $r_0 \sim 24.5 - 26.2$ and $g_0 \sim 25.4 - 27.3$. In Fig. 2 we show the completeness curves in both bands for a pointing taken under good seeing conditions ($\sim 0''.55$), as well as one with poorer seeing ($\sim 1''.00$).

3. GLOBAL RESOLVED STELLAR HALO PROPERTIES

3.1. Global color-magnitude diagram

In Fig. 1 we show the dereddened global color-magnitude diagram (CMD) across the PISCeS survey, containing $\sim 5 \times 10^6$ stellar sources. We bin the CMD into 0.05×0.05 mag pixels in color-magnitude space, and display it in the form of a Hess density diagram (square root scale). In the right panel, we overplot solar-scaled Dartmouth isochrones in the SDSS filter system (Dotter et al. 2008). The models are chosen to have a fixed old age (12 Gyr) and varying $[\text{Fe}/\text{H}]$ (from -2.5 to -1.0 in 0.5 dex steps), to illustrate the position of old red giant branch (RGB) stars at the distance of Cen A.

The contaminant sources are highlighted by this CMD: 1) Galactic foreground stars are distributed in two almost vertical sequences at magnitudes brighter than the tip of the RGB (TRGB) in Cen A, at colors $(g - r)_0 \sim 0.3$ (Galactic halo) and ~ 1.5 (Galactic disk); and 2) unresolved background galaxies are concentrated in a magnitude range similar to that of Cen A RGB stars and blueward of it, i.e., $(g - r)_0 \sim 0.2$. The presence of intermediate-age stellar populations ($\sim 1 - 8$ Gyr) is indicated by asymptotic giant branch (AGB) stars above the TRGB (old AGB stars at these magnitudes are far

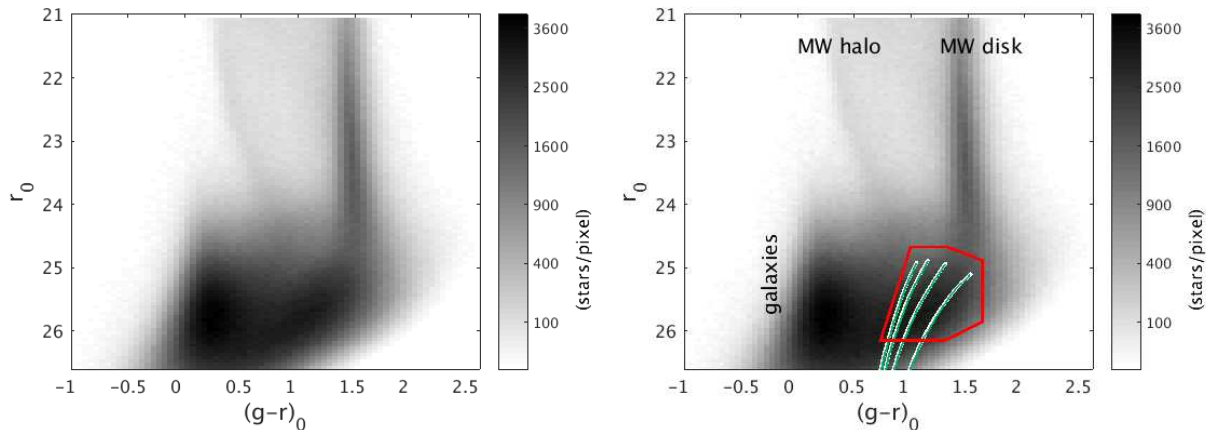


FIG. 1.— *Left panel.* De-reddened Hess diagram of the entire Cen A stellar catalogue to date. The CMD is binned into 0.05×0.05 mag pixels in both magnitude and color and displayed on a square root scale. *Right panel.* We overlay Dartmouth isochrones with a fixed age of 12 Gyr and varying metallicity from $[\text{Fe}/\text{H}] = -2.5$ to -1.0 (from left to right) in 0.5 dex steps, shifted to the distance of Cen A to indicate the position of old RGB stars. The red box indicates our selection for RGB stars, and the accompanying RGB stellar map of Cen A is presented in Fig. 3. The contaminant sequences are clearly identified with respect to the RGB population of Cen A: foreground stars are mostly found above the TRGB at $(g-r)_0 \sim 0.3$ (Galactic halo) and ~ 1.5 (Galactic disk), and their numbers drop significantly at fainter magnitudes, while unresolved background galaxies are concentrated blueward of the RGB around $(g-r)_0 \sim 0.2$.

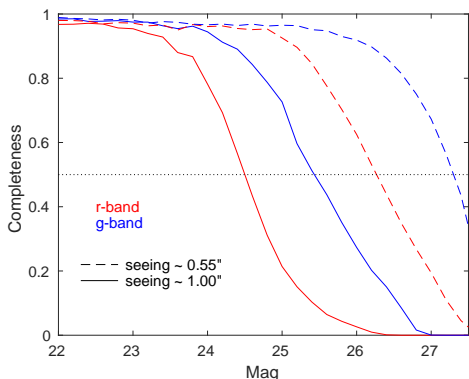


FIG. 2.— Completeness curves in both g - (blue lines) and r -band (red lines) for two pointings within the PISCeS survey taken under different seeing conditions (as indicated). The dotted black line denotes the 50 per cent completeness level.

less numerous); while this region of the CMD is heavily contaminated by Galactic disk stars, they can still be detected as local statistical overdensities with respect to the contaminants. Similarly, unresolved galaxies at blue colors overlap the locus of young massive stars, if they are present. The possible young and intermediate-age populations will not be further quantified in this contribution.

In order to investigate the halo of Cen A and its substructures on such large scales, we have to adopt an RGB selection box that minimizes the fraction of contaminants (see above) and at the same time minimizes the pointing-to-pointing variations due to inevitably varying observing conditions, i.e., photometric incompleteness. We therefore select the red box drawn in Fig. 1, which has the following coordinates: $(g-r)_0 = (0.68, 0.94, 1.27, 1.58, 1.58, 1.25)$ and $r_0 = (26.10, 24.63, 24.63, 24.84, 25.80, 26.10)$. This box encompasses RGB stars with $-2.5 \lesssim [\text{Fe}/\text{H}] \lesssim -0.7$ and reaches ~ 1.2 mag below the metal-poor TRGB ($r_0 = 26.1$). We allow the RGB box to extend ~ 0.3 mag above the TRGB as well (corresponding to a distance ~ 300 kpc closer than the nominal Cen A distance), in order to

take into account possible distance gradients in the halo of Cen A, as well as photometric uncertainties.

3.2. Red giant branch spatial density map

We show the RGB spatial density map of Cen A in Fig. 3, aimed at highlighting the substructure in its extended halo. RGB stars within the selection box drawn in Fig. 1 are binned into 3×3 arcmin² bins (this value was chosen after visual inspection of sample maps produced with a range of bin sizes, with the aim of balancing spatial resolution and homogeneity). In this map we exclude seven additional pointings obtained in 2010, which extend along the minor axis of Cen A in the NW direction, and two separate pointings in the South targeting two known Cen A dwarfs (KK196 and KK203); we will present these data in a future contribution. We also leave out two additional pointings, centered at $(\xi = 1.0^\circ, \eta = 1.9^\circ)$ and $(0.2^\circ, 0.3^\circ)$, because of their low completeness; the latter, in particular, is located in the very central, high density region, which would make its contrast with the adjacent pointings even more apparent. The completeness map for this region is also shown in the same figure, and we derive it by counting the number of recovered fake stars with respect to the number of injected fake stars within the RGB selection box in 3×3 arcmin² spatial bins, for each pointing. The completeness map illustrates the wide range of observing conditions under which these pointings were taken. The RGB map is corrected by weighting the derived RGB star counts in each spatial bin by the relative completeness value, whenever the latter is higher than 20%. For lower completeness values, we increase the stellar density per bin to match the median density of surrounding bins within a $40 < r < 50$ bin annulus.

Our study is the first to contiguously map the extended halo of any elliptical galaxy in resolved stars out to such large galactocentric distances and down to such low surface brightness limits ($\mu_{V,0} \sim 32$ mag arcsec⁻²). This surface brightness limit is an approximate value (i.e., it varies from pointing to pointing) obtained from the field-subtracted surface brightness profiles of the newly

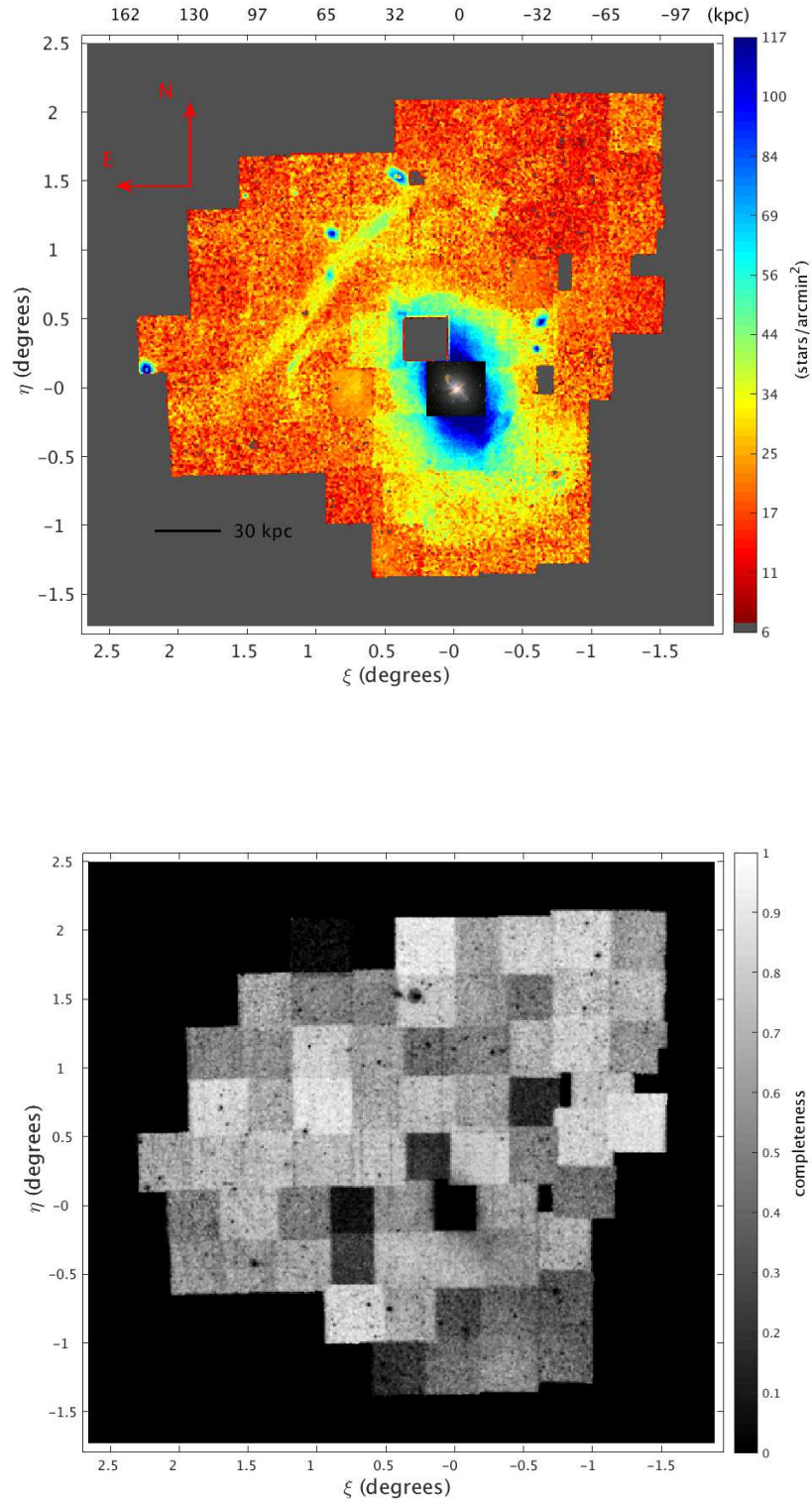


FIG. 3.— *Upper panel.* Density map of Cen A RGB stars, in standard coordinates centered on Cen A. Stars from the red selection box illustrated in Fig. 1 are placed into 3×3 arcmin² bins, and the counts are corrected for incompleteness (see Sect. 3.2 for details). The density scale is shown on the right, while the physical scale is reported on the upper axis. The central pointing is highly incomplete due to extreme stellar crowding, and we replace it with a composite color image of Cen A (credit: ESO/WFI (Optical); MPIFR/ESO/APEX/A.Weiss et al. (Submillimetre); NASA/CXC/CfA/R.Kraft et al. (X-ray); image at <http://www.eso.org/public/images/eso0903a/>). *Lower panel.* Completeness map for the region shown in the upper panel, for stars in the RGB selection box (the central pointing has been omitted). The colorbar covers completeness values from 0% (0) to 100% (1).

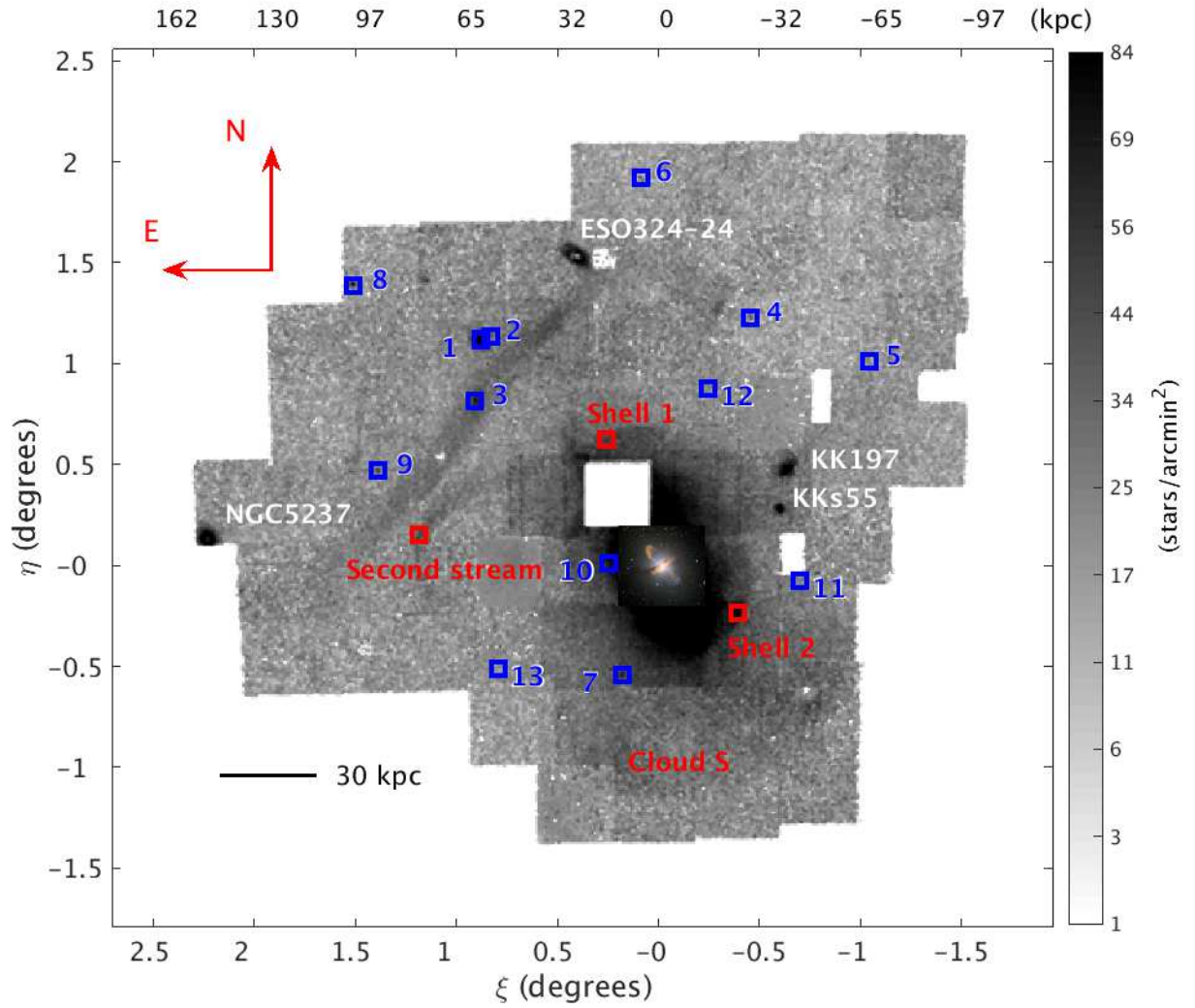


FIG. 4.— Same as the upper panel of Fig. 3: we label our 13 newly discovered dwarf candidates in blue (from CenA-MM-Dw1 to CenA-MM-Dw13, where the label on the plot corresponds to the number of the dwarf), and the 4 previously known dwarfs in white. The red labels indicate the most prominent stream and shell features in the halo of Cen A.

discovered dwarfs (see Sect. 4.1.2). The central regions of Cen A (the innermost $\sim 1 \times 1$ deg² in Fig. 3) have previously been the target of several integrated light studies (see, e.g., Israel 1998; Peng et al. 2002), which expose signs of a recent merger event and of additional shells by tweaking the contrast between surface brightness features. We clearly resolve some of these previously known features into stars, which appear saturated in our RGB map as the contrast was tuned for much fainter features in the outer halo of the galaxy. Even so, a number of newly uncovered shells with embedded overdensities show minor accretion events caught in the act – see positions ($\xi = 0.3^\circ, \eta = 0.6^\circ$) and ($-0.4^\circ, -0.25^\circ$), labeled Shell 1 and Shell 2, respectively, in Fig. 4.

In addition, the unprecedented areal coverage clearly shows the presence of an old, relatively metal-poor population across the whole survey, confirming prior results with smaller fields-of-view (e.g., Crnojević et al. 2013; Rejkuba et al. 2014), along with a plethora of previously unknown streams and substructures. The overdensities in the RGB spatial map not only uncover extremely low surface brightness features, but also allow us to discover very faint dwarfs around Cen A (see also Crnojević et al. 2014b). Within the survey area there are only four previously known dwarfs, i.e., ESO324-24 ($\xi = 0.3^\circ, \eta = 1.6^\circ$), NGC5237 ($2.2^\circ, 0.1^\circ$), KKs55 ($-0.7^\circ, 0.3^\circ$), and KK197 ($-0.75^\circ, 0.5^\circ$) (see, e.g., Karachentsev 2005; Karachentsev et al. 2007), and they are labeled in white in Fig. 4. In the same area, we found 13 dwarf candidates (blue labels), which allow us to significantly extend the faint end of the satellite luminosity function of Cen A (see Sect. 4.3). At the same time, red squares in Fig. 4 are placed on the most prominent new streams and shells in the outer halo of Cen A (see Sect. 4). We will discuss both the satellites and the substructures in the next section, and we additionally show a zoomed-in region of the large RGB map in Fig. 5, focused on the northern portion of the halo of Cen A.

Finally, we stress that the inevitable residual contamination from foreground and background sources in our RGB selection box does not significantly affect the presented density map. We have derived similar maps for the contaminant sources and found them to be smooth overall, and will present these maps in a forthcoming paper on the smooth halo of Cen A vs its accreted substructure.

4. NEWLY DISCOVERED SATELLITES AND HALO SUBSTRUCTURES

Within the current survey footprint, we identified 13 candidate satellites of Cen A and several halo substructures. We first perform a visual inspection on smoothed images, and subsequently complement the search by identifying overdensities in the RGB density map. The location of the new satellites/substructures with respect to Cen A is shown in Fig. 4 (blue and red labels). Of the 13 candidate satellites, we have already presented the pair of dwarfs CenA-MM-Dw1 and CenA-MM-Dw2 in Crnojević et al. (2014b). Seven additional candidates (CenA-MM-Dw3 to CenA-MM-Dw9, named in order of discovery) are robustly confirmed from the unambiguous presence of RGB stars at the distance of Cen A in their CMDs, while four (CenA-MM-Dw10 to CenA-MM-Dw13) are only detected as surface brightness en-

TABLE 1
COORDINATES OF UNRESOLVED DWARF CANDIDATES
(FIG. 4).

Dwarf candidate	RA (h:m:s)	Dec (d:m:s)
Dw10	13:26:49.2	-43:00:00
Dw11	13:21:40.1	-43:04:57
Dw12	13:24:10.9	-42:08:23
Dw13	13:29:51.7	-43:31:10

hancements in the images and do not have a significant resolved counterpart (i.e., we cannot constrain their distances with the method presented in the next subsection). These latter diffuse objects might be Cen A satellites fainter than our detection limit, such that the number of RGB stars in our covered magnitude range is not large enough for them to show up as overdensities, or else they might be background galaxies. We report their positions in Fig. 4 and in Table 1, but we do not consider them further here.

We compute distances for all the newly discovered features in halo of Cen A, and additionally derive surface brightness profiles and structural parameters for the robust new candidate dwarfs. We briefly describe our methods in the following subsection, and then discuss the derived properties of our discoveries in more detail.

4.1. Methods

4.1.1. Distances

Distances throughout this paper are derived with the TRGB method (e.g., Da Costa & Armandroff 1990; Lee et al. 1993; Salaris et al. 2002; Rizzi et al. 2007), as already described in Crnojević et al. (2014b). Briefly, the luminosity of the brightest old, metal-poor RGB stars is nearly constant in red bands, and can thus be used as a standard candle. We employ a Sobel detection filter to highlight the position of the sharp transition in the r -band luminosity function that indicates the TRGB. The luminosity function is corrected for field contamination, and it only includes those stars with colors $0.9 < (g-r)_0 < 1.5$ (corresponding to isochrones with metallicities $[\text{Fe}/\text{H}] = -2.5$ to -1.0) in order to avoid contamination from blue unresolved galaxies. The derived $r_{0,\text{TRGB}}$ values are then transformed into distance moduli by assuming $M_r^{\text{TRGB}} = -3.01 \pm 0.10$ (see Sand et al. 2014); the resulting errors mainly depend on photometric uncertainties and on the TRGB value calibration uncertainty. As we will measure distances to the satellites and to many surface brightness features in our Cen A RGB map, we tabulate all of our results in Table 2 and Table 3, referencing directly the features seen in Fig. 5.

4.1.2. Structural parameters and luminosities

For the candidate dwarfs, we compute the ellipticity and position angle of their RGB stellar distribution with the method of moments, as illustrated in detail in, e.g., Crnojević et al. (2014a). To derive their surface brightness profiles, we sum up the flux of RGB stars from our selection box as a function of projected elliptical radius, correct the results for incompleteness (averaged within the RGB box), divide by the annulus area, subtract the field level as derived from the regions shown in Fig. 5

(see next subsection for details), and convert into surface brightness. In order to account for unresolved light, we furthermore derive the surface brightness of the innermost datapoint (i.e., within a 0.5 arcmin radius for CenA-MM-Dw3, and a 0.2 arcmin radius for the other dwarfs, see Figs. 9–15) via direct aperture photometry on the r -band image. The aperture photometry is performed after masking foreground/background objects, and the median pixel value (i.e., background level) for that image is subtracted. We subsequently shift the first point of the profile derived from individual RGB stars to match the central aperture photometry value. With this method we are able to efficiently trace the extremely low surface brightness in the outer regions of our dwarf targets via resolved RGB stars (see, e.g., Crnojević et al. 2014a). The resulting profiles are shown in the bottom panels of Figs. 9–15. We fit the exponential profiles via least squares minimization to the surface brightness profiles, and obtain values for the half-light radius (r_h) and the central surface brightness ($\mu_{r,0}$, which is translated into $\mu_{V,0}$ by adopting the Jester et al. 2005 conversion factors). Finally, we compute absolute magnitudes by integrating the best-fit exponential profile. All the derived quantities are found in Table 3.

4.2. CenA-MM-Dw3 and its extended tidal tails

The RGB maps of Cen A show a clearly disrupting dwarf galaxy with tidal tails spanning over 1.5 degrees, which we dub CenA-MM-Dw3 (see Figs. 3 and 4). A zoom-in RGB density map of the North-East portion of the survey, containing CenA-MM-Dw3, is presented in Fig. 5. We select the remnant of CenA-MM-Dw3 and a few regions along its stream from the map in Fig. 5 (red polygons) in order to have a closer look at their stellar populations, and we label them e.g., ‘Dw3 S’, ‘Dw3 N’, etc. The central coordinates for the selected regions are reported in Table 2. We extract CMDs for these regions and show them in Figs. 6, 7, 8. Given that the substructures under study have been observed within different Megacam pointings, at different projected distances from the center of Cen A, and under a range of conditions, we will plot the CMD of each one together with a local “field” (i.e., background plus foreground, plus a likely Cen A halo contribution) CMD extracted from the same pointing: the closest blue dashed polygon to each of the red boxes, or an average of the two closest polygons, is adopted as its field (see Fig. 5), appropriately scaled to the target substructure area.

In Fig. 6 we plot the CMD of the main galaxy remnant, which shows a prominent, red RGB. Besides these old stellar populations, CenA-MM-Dw3 also has an over-density of sources above the TRGB which may possibly indicate a population of intermediate-age (a few Gyr), luminous AGB stars. No blue main sequence stars are apparent, indicating no recent star formation.

4.2.1. Distance to CenA-MM-Dw3

The main body of CenA-MM-Dw3 lies 80 kpc in projection from Cen A. For this remnant we find a distance of $r_{0,\text{TRGB}} = 25.31 \pm 0.16$, which translates into a distance modulus of $(m - M)_0 = 28.32 \pm 0.19$. This value implies that CenA-MM-Dw3 is located slightly behind Cen A, at a distance of 4.61 ± 0.42 Mpc. At this

distance, the highest surface brightness portion of the tails of CenA-MM-Dw3 stretches for at least ~ 120 kpc (i.e., ~ 1.5 deg on the sky), or more if they are not co-planar. As a cross-check, we additionally derive the distance modulus of Cen A from our many selected field regions (see Fig. 5), i.e., for stars belonging to the outer halo of Cen A. We obtain a range of values bracketed by $(m - M)_0 = 27.82 \pm 0.19$ and $(m - M)_0 = 28.22 \pm 0.19$ and with a mean value of $(m - M)_0 = 28.03 \pm 0.15$: this is in agreement with the average of literature values obtained via several methodologies ($(m - M)_0 = 27.91 \pm 0.05$; Harris et al. 2010). Adopting the mean distance value to Cen A from our dataset, the 3D distance of CenA-MM-Dw3 to Cen A is 580 ± 500 kpc.

The distances of CenA-MM-Dw3 and Cen A itself are consistent to within 2σ . Nonetheless, we consider the possibility of the latter not being the main disturber of CenA-MM-Dw3. The next closest relatively massive galaxy is NGC5408 ($M_V \sim -17.0$), an irregular galaxy located at 4.8 ± 0.5 Mpc and ~ 6 deg away from CenA-MM-Dw3 (Karachentsev et al. 2007). The 3D distance between CenA-MM-Dw3 and NGC5408 is 530 ± 200 kpc. While not significantly different from the distance between CenA-MM-Dw3 and Cen A, the latter is much more massive and is thus more plausibly the culprit for the heavy tidal disruption experienced by our target. In addition, the radial velocity of NGC5408 is lower than that of Cen A by $\sim 10\%$, such that a radial velocity measurement for CenA-MM-Dw3 might help solve this question. Only detailed simulations will be able to shed light onto these possibilities. If Cen A is indeed the main perturber of CenA-MM-Dw3, the morphology of this long stream can additionally constrain the dark matter halo mass of Cen A (e.g., Amorisco 2015; Pearson et al. 2015).

4.2.2. Distances along the stream of CenA-MM-Dw3

We further characterize the properties of CenA-MM-Dw3 by deriving distances along its stream. We select two regions to the South-East (dubbed Dw3 S and SE in Fig. 5), a region encompassing the higher density feature along its northern elongation (Dw3 N), a region located in the same direction and just South of the dwarf galaxy ESO324-24 (ESO324-24 S), and the very low density region to the far North-West of CenA-MM-Dw3 (Dw3 NW).

The CMDs of Dw3 S, Dw3 SE and Dw3 NW are shown in Fig. 7. Despite a varying completeness level, the RGBs in these regions are comparable to the one shown in Fig. 6 for the remnant of CenA-MM-Dw3. We derive TRGB values and distance moduli as follows: $r_{0,\text{TRGB}} = 25.17 \pm 0.19$ and $(m - M)_0 = 28.18 \pm 0.21$ for Dw3 S, $r_{0,\text{TRGB}} = 25.08 \pm 0.16$ and $(m - M)_0 = 28.09 \pm 0.19$ for Dw3 SE, $r_{0,\text{TRGB}} = 25.11 \pm 0.17$ and $(m - M)_0 = 28.12 \pm 0.19$ for Dw3 N. The derived values are all consistent with each other, and with the distance modulus of CenA-MM-Dw3 within the errorbars ($(m - M)_0 = 28.32 \pm 0.19$).

Given the proximity of the northwestern portion of the stream to the dwarf irregular ESO324-24 ($M_B \sim -14.9$; Côté et al. 2009), we investigate a possible spatial overlap in their stellar populations. ESO324-24 presents a perturbed HI morphology: its asymmetric gas tail (pointing towards the NE), together with its gas kinematics, suggest it is undergoing ram pressure stripping from the northern radio lobe of Cen A (Johnson et al.

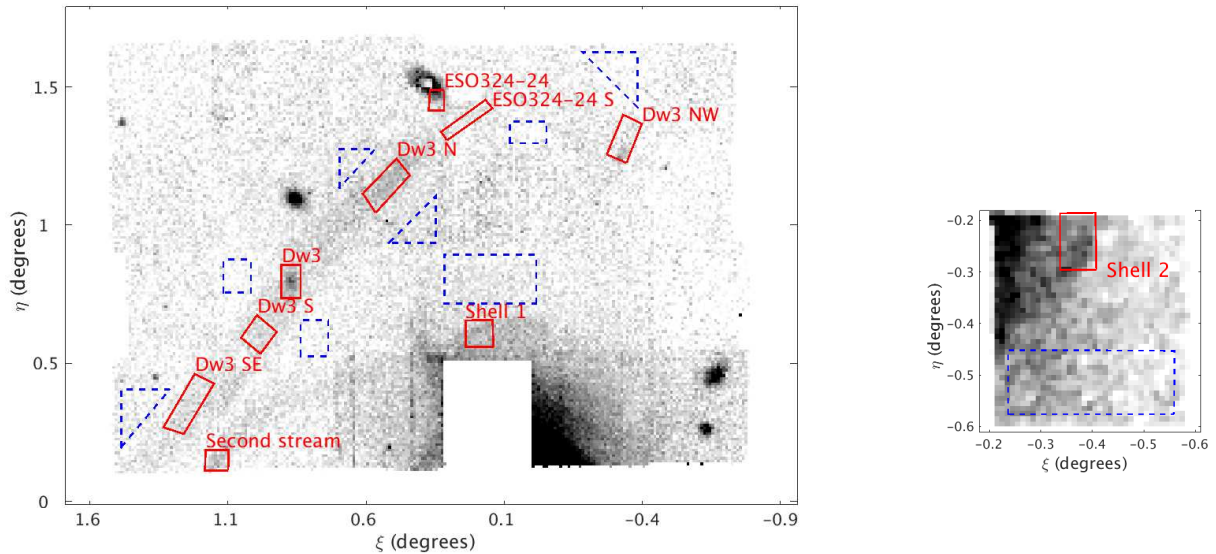


FIG. 5.— *Left panel.* RGB density map for a zoomed-in region containing the most prominent substructures discovered in the northern portion of the survey (see Fig 4 and Sect. 4). Red boxes indicate the regions for which CMDs are drawn in Fig. 9–16; blue dashed boxes indicate the field regions chosen on a pointing-to-pointing basis for the red boxes. *Right panel.* Same as left panel, for the pointing containing Shell 2 (located to the South-West of the center in Fig. 4).

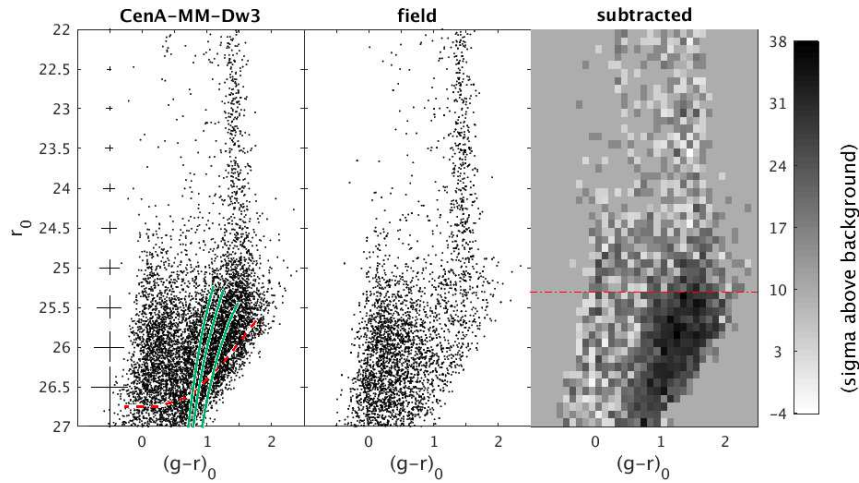


FIG. 6.— Dereddened color-magnitude diagram for CenA-MM-Dw3 (region labeled as Dw3 in Fig. 5). We overplot isochrones shifted to the measured distance of the dwarf, with a 12 Gyr age and metallicities $[\text{Fe}/\text{H}] = -2.0, -1.5$ and -1.0 (from left to right). The red dashed line indicates the 50% completeness level, and photometric errors as derived from artificial star tests are drawn on the left side of the CMD. A background field CMD drawn from the same pointing (dashed blue rectangles next to Dw3 in Fig. 5) and rescaled to the box area of CenA-MM-Dw3 is shown for comparison in the *middle panel*. The *right panel* is a Hess diagram of the CMD of CenA-MM-Dw3 after background subtraction. The red dot-dashed line indicates the derived TRGB magnitude.

2015). However, its resolved stellar content does not reveal clear signs of distortion. The CMDs we discuss are shown in Fig. 8. First, we compute the distance for a region in the outskirts of ESO324-24: in this way we avoid the high density central regions (stellar crowding is the culprit for the hole seen at the center of this galaxy, see e.g., Fig. 5), as well as the most recent star formation pockets closer to the central parts of this dwarf (e.g., Côté et al. 2009). We obtain $r_{0,\text{TRGB}} = 24.90 \pm 0.16$ and $(m - M)_0 = 27.91 \pm 0.19$, in good agreement with the $(m - M)_0 = 27.84 \pm 0.05$ listed in Jacobs et al. (2009). The stream portion below ESO324-24 (ESO324-24 S) has $r_{0,\text{TRGB}} = 25.18 \pm 0.19$, thus $(m - M)_0 = 28.19 \pm 0.20$,

which is slightly closer to the rest of the stream rather than to the values of ESO324-24. This suggests that this low surface brightness elongation is not associated with the latter, but with CenA-MM-Dw3. The lack of further density enhancements on the opposite side of ESO324-24, or of obvious signs of distortion in its main body, support this interpretation. Finally, for the north-western overdensity (Dw3 NW) we obtain $r_{0,\text{TRGB}} = 24.81 \pm 0.17$, thus $(m - M)_0 = 27.82 \pm 0.19$: this feature is closer (along the line of sight) than, and probably does not belong to, the stream of CenA-MM-Dw3.

4.2.3. Structural parameters and luminosity

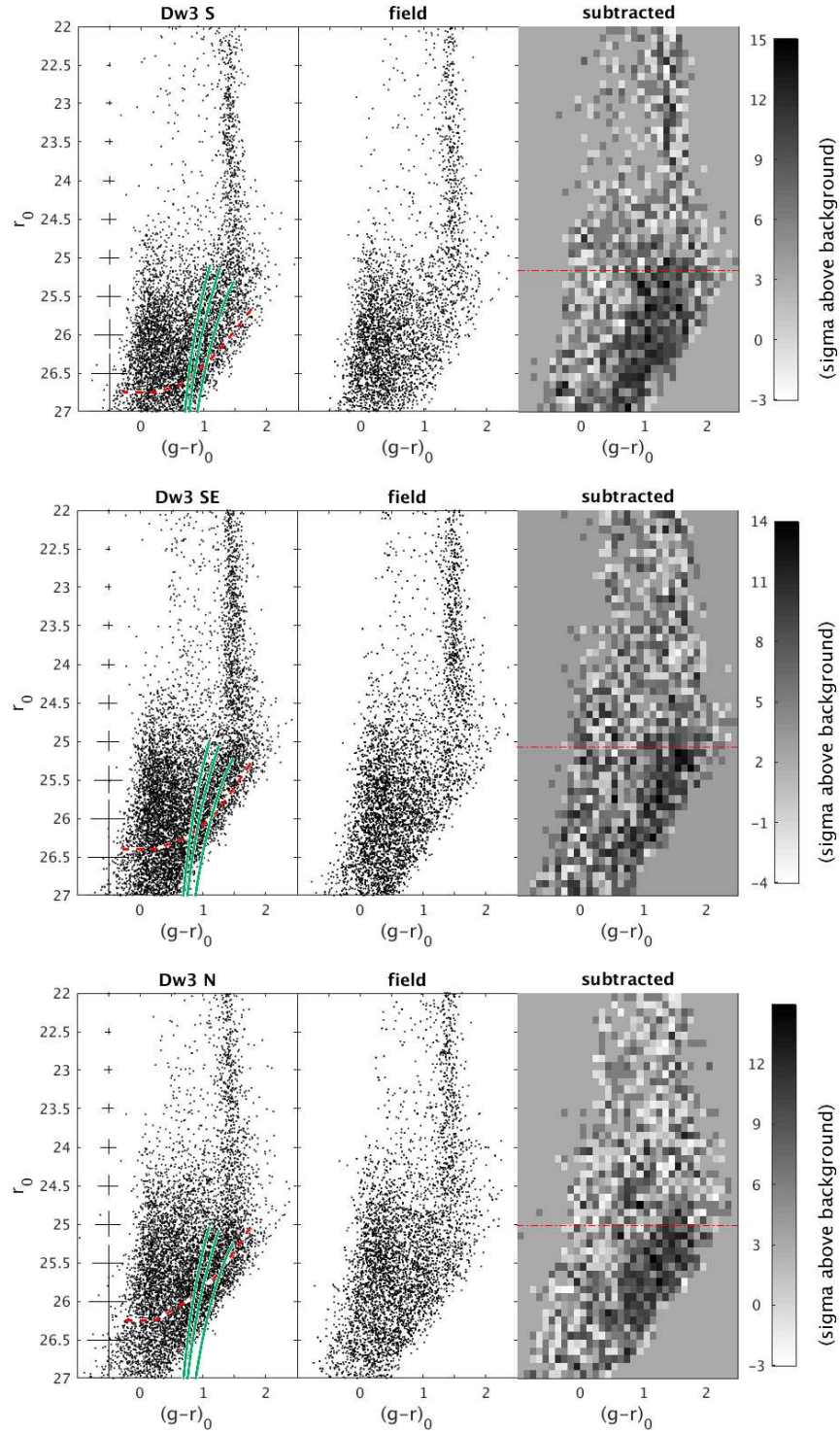


FIG. 7.— Dereddened color-magnitude diagrams for three regions along the stream of CenA-MM-Dw3 (rectangles labeled Dw3 S, Dw3 SE, Dw3 N in Fig. 5). The panels are the same as in Fig. 6, while the incompleteness levels, photometric uncertainties and adopted field regions change on a pointing-to-pointing basis. The TRGB is recomputed for each of the selected regions and the isochrones are shifted to the appropriate distance. The selected stream regions are consistent with the distance found for CenA-MM-Dw3.

TABLE 2
CENTRAL COORDINATES OF AND DISTANCES TO HALO SUBSTRUCTURES (SEE FIG. 5).

Substructure	RA (h:m:s)	Dec (d:m:s)	$(m - M)_0$ (mag)	D (Mpc)
Cen A ^a	13:25:27.6	-43:01:09	27.91 ± 0.05	3.80 ± 0.10
Cen A (this work)	–	–	28.03 ± 0.15	4.04 ± 0.29
CenA-MM-Dw3	13:30:21.5	-42:11:33	28.32 ± 0.19	4.61 ± 0.42
Dw3 S	13:31:02.6	-42:21:54	28.18 ± 0.21	4.33 ± 0.44
Dw3 SE	13:32:18.0	-42:36:54	28.09 ± 0.19	4.15 ± 0.44
Dw3 N	13:28:27.6	-41:51:00	28.12 ± 0.19	4.20 ± 0.39
ESO324-24	13:27:32.4	-41:33:00	27.91 ± 0.19	3.82 ± 0.36
ESO324-24 S	13:27:03.6	-41:37:30	28.19 ± 0.20	4.35 ± 0.41
Dw3 NW	13:23:57.6	-41:42:00	27.82 ± 0.19	3.66 ± 0.34
Second stream	13:31:54.0	-41:51:00	28.03 ± 0.19	4.04 ± 0.37
Shell 1	13:26:45.6	-42:22:30	28.43 ± 0.20	4.75 ± 0.46
Shell 2	13:23:21.6	-43:14:06	28.20 ± 0.20	4.36 ± 0.40

^a Value from Harris et al. (2010).

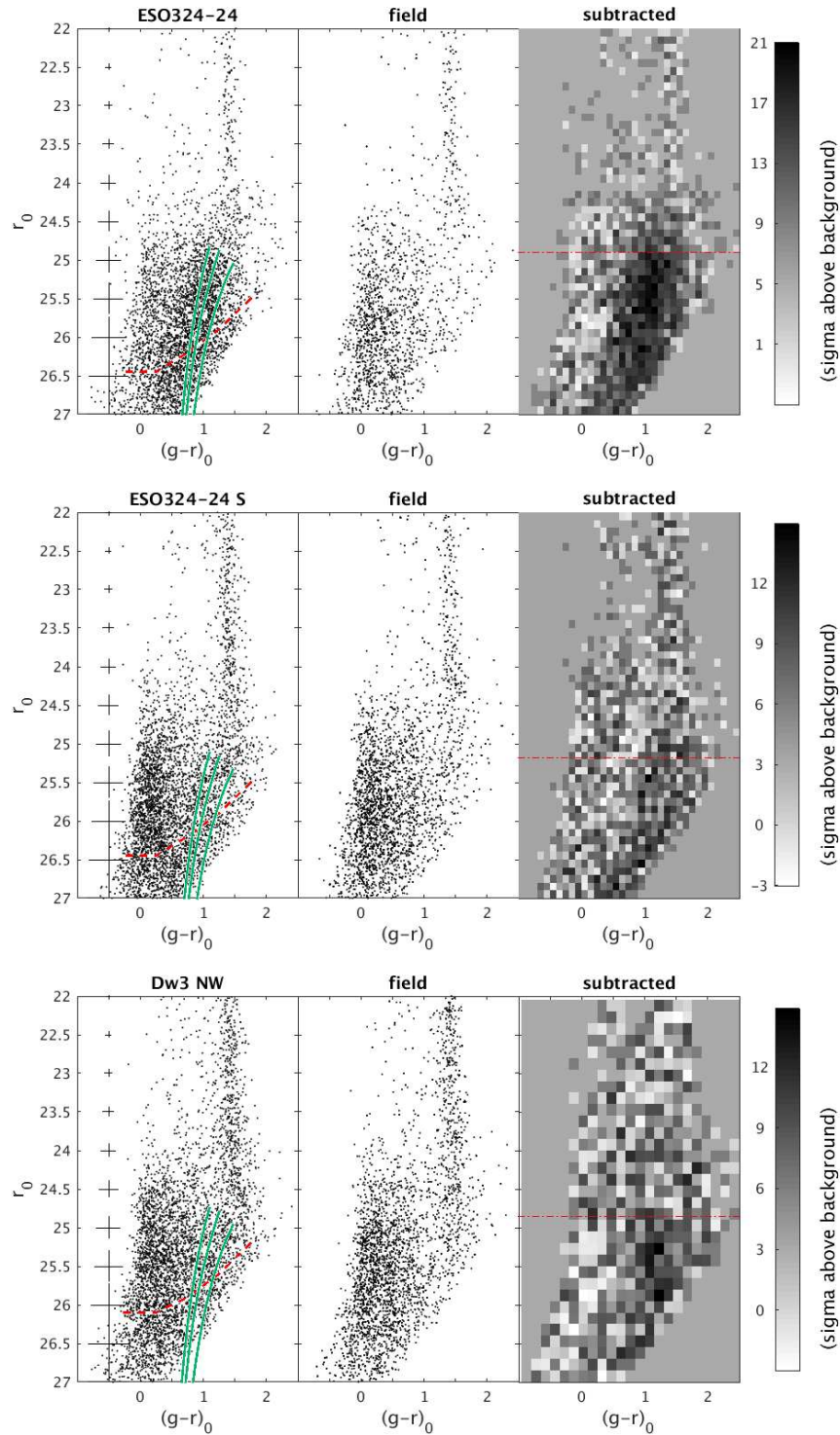


FIG. 8.— CMDs for the previously known Cen A satellite ESO324-24 and for two stream regions located to its immediate South and to its far West (see Fig. 5). Note that the adopted color/magnitude bins for the subtracted Hess diagram of Dw3 NW are larger than for the other regions because of low counts. Based on the difference in the derived TRGB values, we argue that the region immediately to the South of ESO324-24 still belongs to the stream of CenA-MM-Dw3, while the region to the North-West might constitute a separate tidal feature in the halo of Cen A.

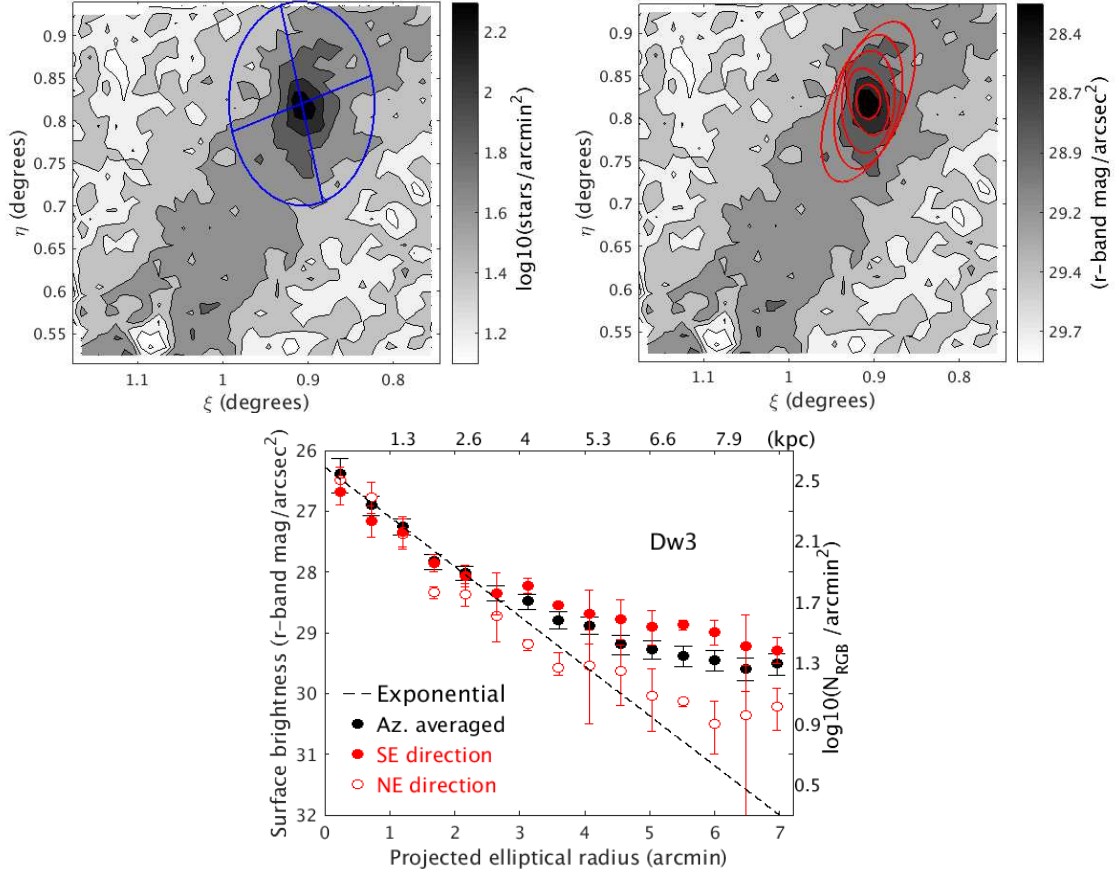


FIG. 9.— *Upper panels.* Density map of CenA-MM-Dw3 RGB stars, after completeness correction. The color scales indicate RGB stellar density (*left*) and *r*-band surface brightness (*right*). The left panel shows the four azimuthal wedges that divide the remnant of CenA-MM-Dw3 into “tidal tail-free” (NE and SW) and “tidal tail” (NW and SE) regions. For the right panel, position angle and ellipticity are recomputed for radial annuli with semimajor axis lengths of 1.2, 2.4, 3.6, 4.8, and 6.0 arcmin and red ellipses are drawn accordingly. *Lower panel.* Surface brightness profiles in *r*-band for CenA-MM-Dw3, where the average ellipticity has been adopted (see Table 3). The azimuthally-averaged profile is shown with filled black points, while the profiles derived in two different directions (SE and NE wedges, see upper left panel) are shown with red symbols, filled for the tidal-tail wedge and hollow for the wedge perpendicular to that. The profiles have been corrected for incompleteness and the field level has been subtracted. The best-fit exponential profile is indicated with a black dashed line and only fits datapoints within the innermost 3 arcmin to avoid the tidal tails.

We draw RGB isodensity contour maps (after incompleteness correction) of the pointing containing CenA-MM-Dw3 in the upper panels of Fig. 9. The adopted RGB selection box is similar to the one drawn in Fig. 1, but slightly adjusted to follow the 50% completeness limits for this pointing (the color-averaged values are $r_0 \sim 26.2$ and $g_0 \sim 26.9$).

We compute the ellipticity and position angle as a function of radius for the remnant of CenA-MM-Dw3. The derived values are adopted to draw ellipses for increasingly large annuli centered on CenA-MM-Dw3 (see Fig. 9). While the main body of the remnant appears almost circular, the outer annuli show a progressive elongation culminating in the tidal tails, and the major axis of the stellar distribution twists to end up almost perpendicularly to the direction of the main body. In Table 3 we report the average ellipticity derived for the innermost 2 arcmin of the galaxy.

To derive a surface brightness profile, we first subdivide the galaxy into four wedges with the same area, two of which are aligned with the tails. We then derive an azimuthally averaged surface brightness profile, as well as profiles in two directions, one along and one perpendicular to the tails (SE and NE wedges, respectively, in the upper left panel of Fig. 9). The resulting profiles are shown in the bottom panel of Fig. 9. The SE and NE profiles remain comparable to each other out to a radius of ~ 2.5 arcmin, beyond which the SE profile (i.e., the tidal tail direction) consistently remains above the NE one. The exponential profile is a good fit to the “unperturbed” surface brightness profile (even though it clearly underestimates the global profile) and returns a very large half-light radius ($r_h = 2.92 \pm 0.20$ kpc) together with a remarkably low central surface brightness ($\mu_{r,0} = 26.3 \pm 0.1$ mag arcsec $^{-2}$, or $\mu_{V,0} = 26.7 \pm 0.1$ mag arcsec $^{-2}$). The absolute magnitude of CenA-MM-Dw3 is obtained as $M_V = -13.0 \pm 0.4$, which is comparable to that of the disrupting MW satellite Sagittarius ($M_V = -13.5 \pm 0.4$). Given the advanced state of disruption of this galaxy, this luminosity is likely much less than the undisrupted luminosity of the galaxy.

As a rough estimate of CenA-MM-Dw3’s original luminosity, we quantify the number of RGB stars along its tails, approximately in between the Dw3 SE and the ESO324-24 S boxes (see Fig. 5). This number is ~ 8 times higher than the number of RGB stars in the Dw3 box: assuming that the tails entirely belong to CenA-MM-Dw3, this implies that its total unperturbed magnitude might have been ~ 2 mag brighter than our estimate for the remnant (i.e., $M_V \sim -15.0$).

4.3. Properties of the most robust newly discovered satellites

In this subsection, we present the discovery CMDs, stellar spatial distributions and structural properties for our six robust new satellite discoveries, besides CenA-MM-Dw1, CenA-MM-Dw2 and CenA-MM-Dw3. Their derived properties are listed in Table 3.

The CMDs of the newly discovered dwarfs show predominantly old populations, and none of them presents significant signs of more recent star formation (i.e., blue stars or luminous AGB stars; upper panels in Figs. 10–15). Their RGBs are consistent with relatively metal-

poor isochrones (indicatively $[\text{Fe}/\text{H}] \sim -2.0 / -1.5$), even though the low number of detected stars renders a more precise quantification difficult from this dataset. Because of the sparsity of their RGBs, for each of these six dwarfs we also report their luminosity functions convolved with the Sobel filter (see Sect. 4.1.1) alongside their CMDs. In most cases this returns a clear maximum which corresponds to the TRGB, however for CenA-MM-Dw5 (the least populated in the sample) the luminosity function presents two comparable maxima. We take the TRGB value to be the average of the maxima’s magnitudes, which translates into a larger uncertainty in CenA-MM-Dw5’s distance (see Table 3).

As for CenA-MM-Dw3, we find exponential profiles to be a good fit for all the other dwarfs (lower panels in Figs. 10–15). From the exponential profiles we derive their absolute magnitudes, which cover three magnitudes, from $M_V = -7.2$ (CenA-MM-Dw5) to -9.8 (CenA-MM-Dw4). The best-fit profiles also return values for their central surface brightness ($\mu_{V,0} = 25.4 - 26.9$ mag arcsec $^{-2}$) and half-light radii ($r_h = 0.22 - 0.58$ kpc). None of these galaxies are visible in Digitized Sky Survey (DSS) images because of their low central surface brightness and/or luminosity.

Within these six newly discovered dwarfs, three objects are relatively small and compact ($r_h < 0.31$ arcmin, or $r_h < 0.35$ kpc), namely CenA-MM-Dw4, CenA-MM-Dw5 and CenA-MM-Dw6. The magnitude, half-light radius, and surface brightness of CenA-MM-Dw4 are comparable to those of Carina, AndV, and AndXVII in the LG (see McConnachie 2012, for LG dwarfs’ properties). The properties of CenA-MM-Dw5 closely compare to those of AndXIII and AndXXVI; this is the faintest PISCeS discovery among our dwarf candidates’ sample, as well as the least luminous galaxy discovered beyond the LG, with $M_V = -7.2$ and $\mu_{V,0} = 26.9$ mag arcsec $^{-2}$. CenA-MM-Dw6 is similar in its properties to AndX and AndXXVIII.

The remaining three dwarfs, CenA-MM-Dw7, CenA-MM-Dw8 and CenA-MM-Dw9, are distinguished by fairly large half-light radii ($r_h > 0.37$ arcmin, or $r_h > 0.36$ kpc), and they all have elongated shapes. In particular, CenA-MM-Dw7, despite having a similar luminosity to that of CenA-MM-Dw6, has a surface brightness one magnitude lower and a half-light radius almost twice as large, and it is comparable to CVnI, AndIX and AndXXVII. Given its proximity to the center of Cen A (it is the closest dwarf in projection from our sample) and its rather elongated shape (Fig. 13), CenA-MM-Dw7 might be in the process of being tidally affected by its giant host, even though our density maps/surface brightness profile do not reveal any signs of structure around the main body of CenA-MM-Dw7 (the significant contamination from the halo of Cen A stars at the position of CenA-MM-Dw7 is however evident from its CMD). The luminosity, surface brightness and half-light radius of CenA-MM-Dw8 closely resemble the recently discovered AndXXV and AndXXI; this dwarf is both brighter ($M_V = -9.7$) as well as more diffuse ($r_h = 0.58$ kpc for $\mu_{V,0} = 26.6$ mag arcsec $^{-2}$) than CenA-MM-Dw7 and CenA-MM-Dw9. Finally, CenA-MM-Dw9 and AndXIV have similar properties.

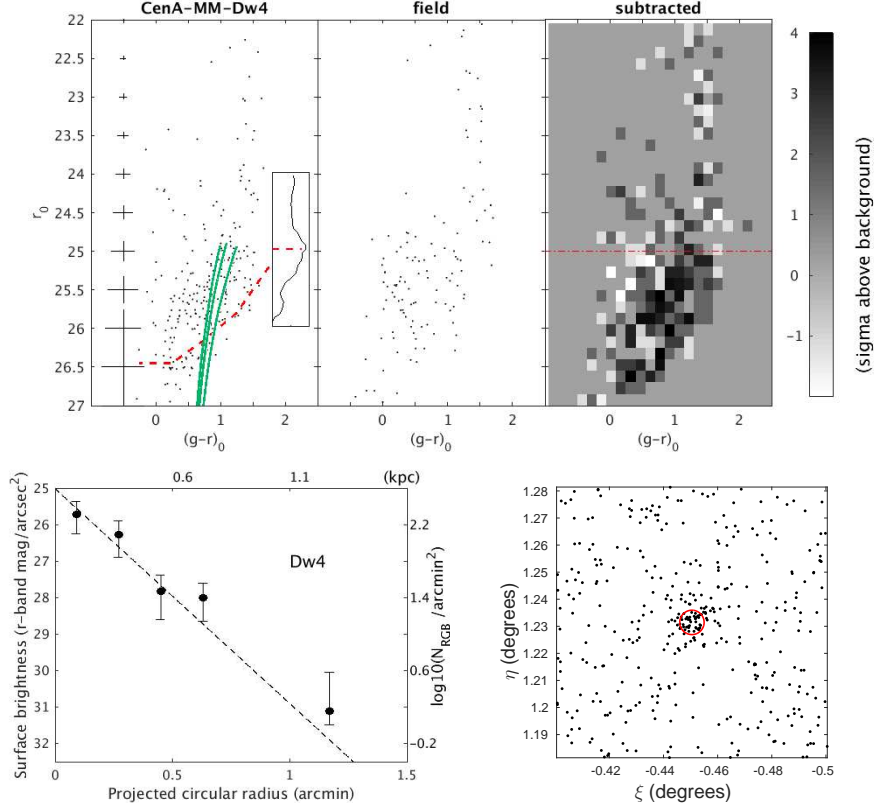


FIG. 10.— *Upper panels.* Dereddened color-magnitude diagram for stars within a box of 0.6×0.6 arcmin² centered on CenA-MM-Dw4 (*left panel*). The isochrones are shifted to the measured distance of the dwarf, with a 12 Gyr age and metallicities $[\text{Fe}/\text{H}] = -2.5$, -2.0 and -1.5 . The red dashed line indicates the 50% completeness level, and photometric errors as derived from artificial star tests are drawn on the left side of the CMD. The inset plot shows the luminosity function after convolution with a Sobel filter, and the derived TRGB magnitude in the *middle panel*. The *right panel* is a background-subtracted Hess diagram. The red dot-dashed line indicates the derived TRGB magnitude. *Lower left panel.* Surface brightness profile in r -band as a function of radius. The profile has been corrected for incompleteness and the field level has been subtracted. The best-fit exponential profile is indicated with a black dashed line. *Lower right panel.* 3×3 arcmin² cutout of the RGB stars spatial distribution in the Magellan/Megacam pointing containing CenA-MM-Dw4, centered on the dwarf. The red circle is at the dwarf's half-light radius.

TABLE 3
PROPERTIES OF THE NEWLY DISCOVERED DWARFS.

Parameter	Dw3	Dw4	Dw5	Dw6	Dw7	Dw8	Dw9
RA (h:m:s)	13:30:21.5±1 ^a	13:23:02.6±1 ^a	13:19:52.4±1 ^a	13:25:57.7±1 ^a	13:26:28.7±1 ^a	13:33:34.1±1 ^a	13:33:01.5±1 ^a
Dec (d:m:s)	-42:11:33±9 ^a	-41:47:11±8 ^a	-41:59:38±9 ^a	-41:05:39±9 ^a	-43:33:25±9 ^a	-41:36:29±8 ^a	-42:31:49±9 ^a
$(m - M)_0$ (mag)	28.32 ± 0.19	27.96 ± 0.25	27.67 ± 0.38	27.78 ± 0.22	27.65 ± 0.19	27.70 ± 0.20	27.90 ± 0.20
D (Mpc)	4.61 ± 0.42	3.91 ± 0.48	3.42 ± 0.65	3.61 ± 0.38	3.38 ± 0.32	3.47 ± 0.33	3.81 ± 0.36
ϵ	0.29 ± 0.19	<0.30 ^c	<0.61 ^c	<0.56 ^c	0.28 ± 0.14	0.26 ± 0.22	0.13 ± 0.12
r_h (arcmin)	2.21 ± 0.15	0.31 ± 0.08	0.21 ± 0.04	0.29 ± 0.01	0.37 ± 0.10	0.60 ± 0.06	0.39 ± 0.02
r_h (kpc)	2.92 ± 0.20 ^a	0.35 ± 0.10	0.22 ± 0.04	0.30 ± 0.01	0.36 ± 0.09	0.58 ± 0.05	0.42 ± 0.03
$\mu_{r,0}$ (mag arcsec ⁻²)	26.3 ± 0.1	25.0 ± 0.5	26.5 ± 0.5	25.5 ± 0.1	26.3 ± 0.7	26.2 ± 0.3	26.1 ± 0.2
$\mu_{V,0}$ (mag arcsec ⁻²)	26.7 ± 0.1	25.4 ± 0.7	26.9 ± 0.7	25.9 ± 0.1	26.7 ± 0.9	26.6 ± 0.4	26.6 ± 0.3
M_V (mag)	-13.0 ± 0.4 ^b	-9.8 ± 1.1	-7.2 ± 1.0	-9.0 ± 0.4	-8.6 ± 1.3	-9.7 ± 0.5	-9.1 ± 0.4
L_* ($10^5 L_\odot$)	129.2 ± 44.3	6.8 ± 8.4	0.6 ± 0.7	3.4 ± 1.1	2.4 ± 3.4	6.7 ± 3.5	3.6 ± 1.4
M_{HI}^d ($10^6 M_\odot$)	$\lesssim 5.7$	$\lesssim 4.6$	$\lesssim 3.6$	$\lesssim 3.4$	$\lesssim 4.2$	$\lesssim 2.3$	$\lesssim 4.4$
M_{HI}/L_* (M_\odot/L_\odot)	$\gtrsim 0.4$	$\gtrsim 6.8$	$\gtrsim 59.7$	$\gtrsim 10.0$	$\gtrsim 17.4$	$\gtrsim 3.4$	$\gtrsim 12.3$

^a This is an indicative value only, since the studied galaxy is being heavily disrupted.

^b Excluding tidal tails.

^c Only upper limits on the ellipticity, ϵ , were measurable.

^d 5σ upper limits from HIPASS.

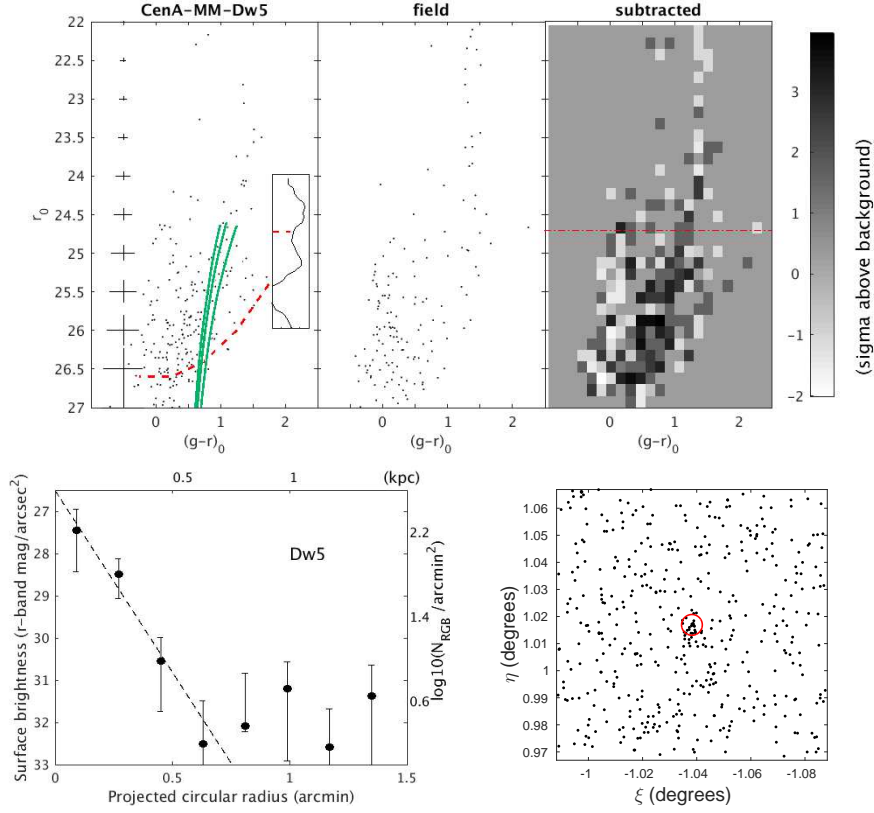


FIG. 11.— Same as Fig 10, for CenA-MM-Dw5. In this case the luminosity function presents two comparable maxima, thus we take the TRGB to be the average of their values.

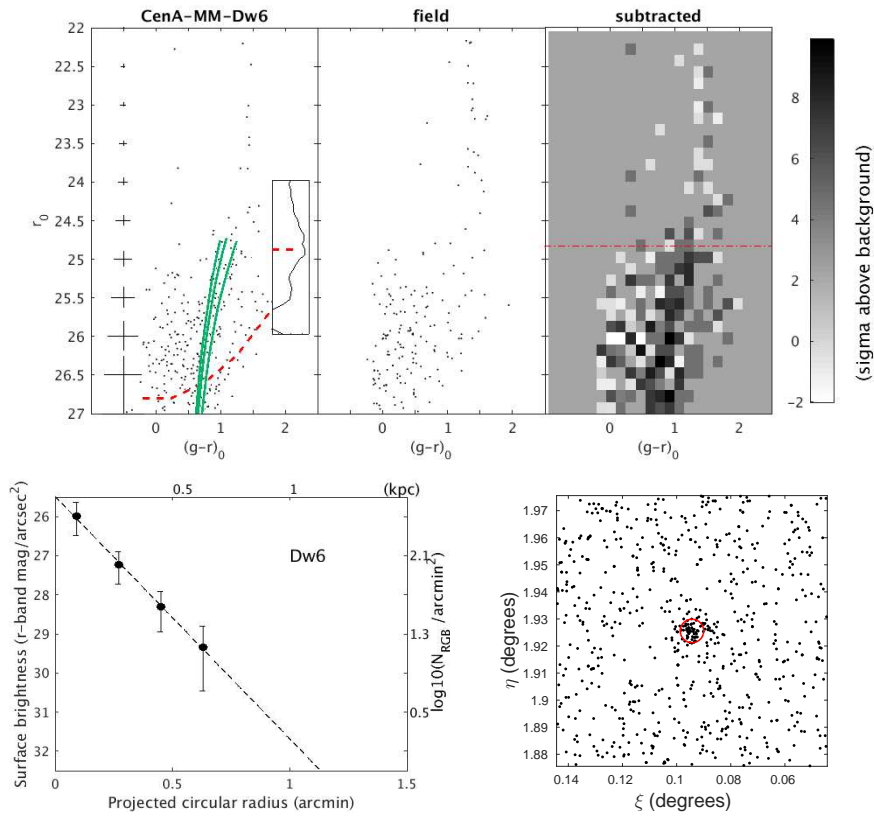


FIG. 12.— Same as Fig 10, for CenA-MM-Dw6.

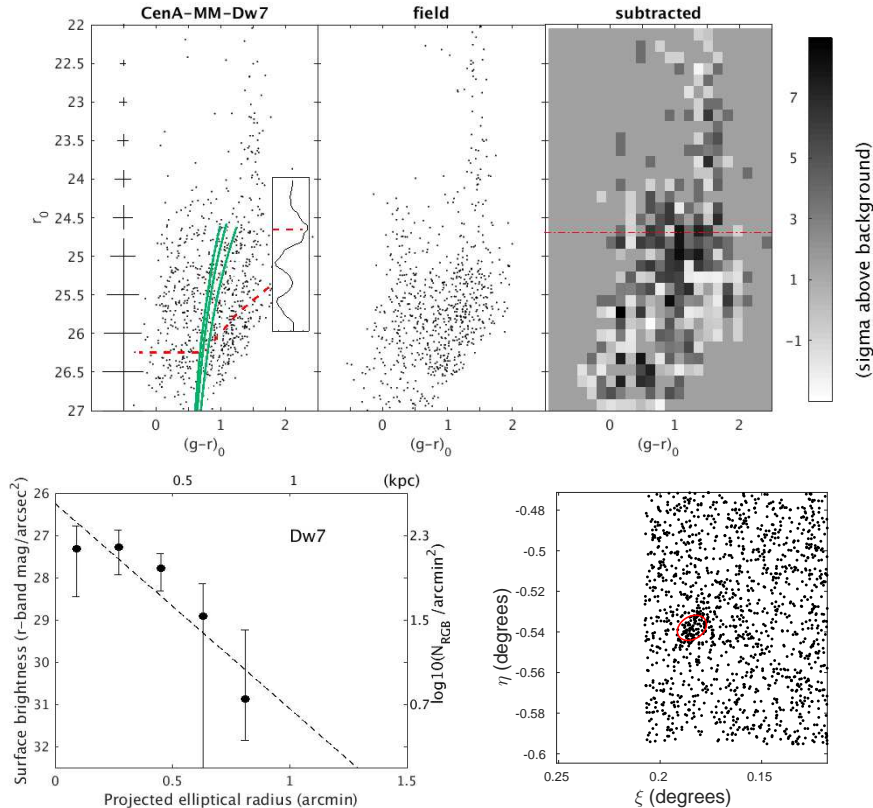


FIG. 13.— Same as Fig 10, for CenA-MM-Dw7. The dwarf CMD contains stars within a box of 0.9×0.9 arcmin² centered on CenA-MM-Dw7, and the RGB spatial distribution is shown for a 4×4 arcmin² region. The contamination from Cen A halo stars is very strong for this dwarf and thus its CMD appears washed out.

4.4. Additional shells and streams

Besides the prominent tidal structure of CenA-MM-Dw3, the halo of Cen A hosts a variety of other previously unknown overdensities. We focus on four of them, as selected from Figs. 4 and 5 (coordinates for these features are found in Table 2).

Second stream. This stream is clearly identified to the East of the main body of Cen A, and South of CenA-MM-Dw3. This stream, thinner with respect to the tails of CenA-MM-Dw3, does not host a clear compact remnant. We draw a CMD from its densest portion (upper panel of Fig. 16), which might contain what is left of its progenitor. At this point, the stream seems to bend back towards Cen A, and significantly drops in stellar density. On the opposite end, the stream points towards the northern part of the Cen A major axis overdensity (Crnojević et al. 2013) but fades before reaching it, such that a possible connection between the two substructures cannot be assessed. With the TRGB method described in Sect. 4.1.1, we derive the distance to this second stream, finding $r_{0,\text{TRGB}} = 25.02 \pm 0.16$, or $(m - M)_0 = 28.03 \pm 0.19$. From its CMD, the second stream seems to host an old RGB without the presence of younger populations. We argue that the progenitor of this second stream must have not been very massive, and its remnant may be already stretched to the point that we cannot recognize any signs of its original appearance.

Shell 1. We call the feature directly to the North of Cen A Shell 1, which becomes apparent to the West of the major axis and assumes a loop-like shape for

~ 0.25 deg. The substructure apparently does not extend beyond this one pointing, but this may be due to incompleteness effects. The adjacent pointing to its West has a lower completeness, but even after our incompleteness correction (see Fig. 5) the Shell 1 structure does not seem to be detected further in this direction. The CMD in Fig. 16 shows a very high stellar density, such that crowding introduces significant incompleteness. The RGB along Shell 1 appears broad, likely extending to large colors/metallicities given the rapidly dropping completeness. The TRGB is found at $r_{0,\text{TRGB}} = 25.42 \pm 0.17$, giving $(m - M)_0 = 28.43 \pm 0.20$, a difference of $\sim 2.5 \sigma$ from the distance of Cen A, but this value requires confirmation due to the high uncertainty.

Shell 2. Located directly to the West of the center of Cen A, Shell 2 resembles the shape of Shell 1. We can trace this substructure extending North from its highest density point (a possible remnant, see Figs. 3 and 5), the latter being clearly separated by a density gap from the inner halo of Cen A and running parallel to it. Beyond this pointing, the shape of Shell 2 becomes less defined and constitutes a lower density “envelope” to the smooth component of Cen A, but it does retain a sharp break with respect to the region to its immediate West (see Fig. 3). The CMD for Shell 2 returns $r_{0,\text{TRGB}} = 25.19 \pm 0.17$, and $(m - M)_0 = 28.20 \pm 0.20$. As for Shell 1, the incompleteness due to crowding is high at this galactocentric distance.

Cloud S. We additionally detect a stellar density enhancement to the South of Cen A, i.e., a broad cloud-like structure extending from $\xi \sim -0.8^\circ$ to $+0.4^\circ$ at $\eta \sim -1^\circ$,

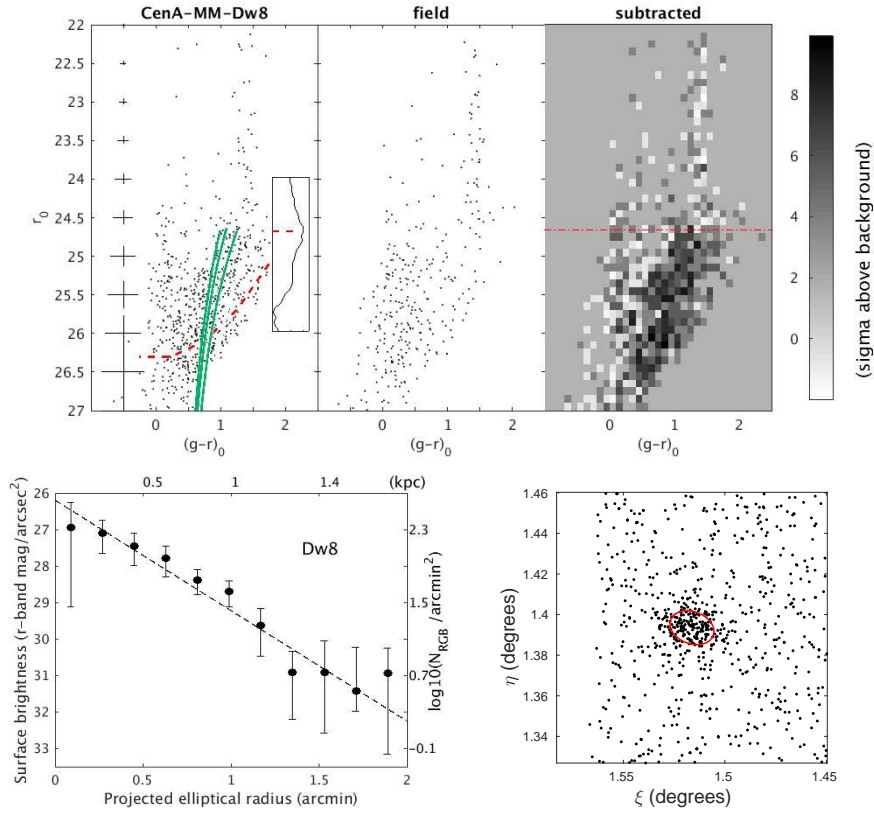


FIG. 14.— Same as Fig 13, for CenA-MM-Dw8.

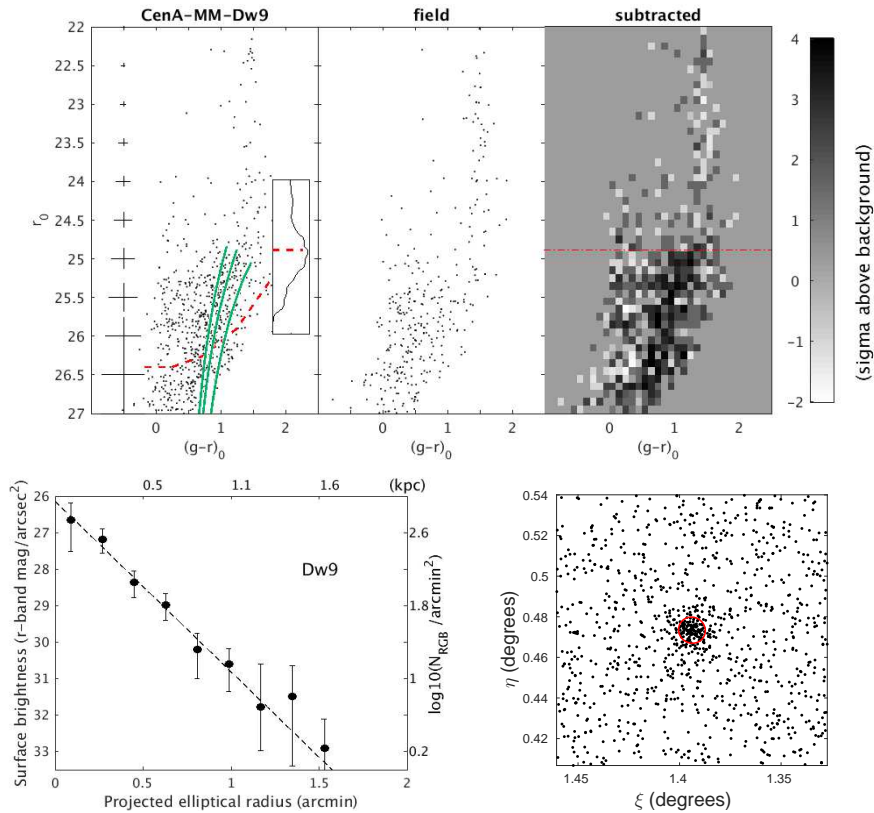


FIG. 15.— Same as Fig 13, for CenA-MM-Dw9.

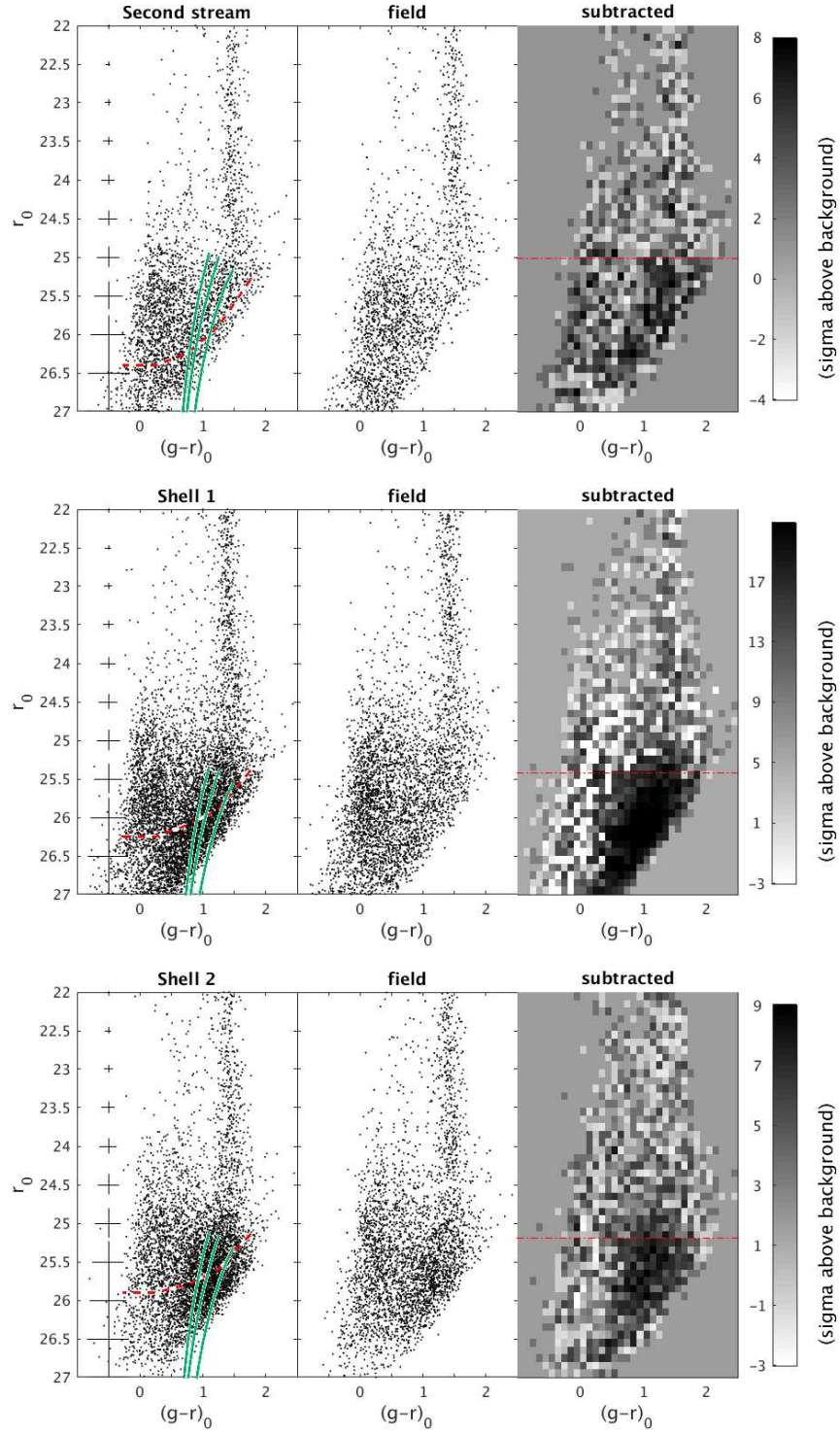


FIG. 16.— Further CMDs of prominent Cen A halo substructures: the apparently progenitor-less Second stream and the shells located to the North of Cen A (Shell 1) and to its South-West (Shell 2; see Fig. 5).

which we call Cloud S (labeled in Fig. 4). The stellar density with respect to the background halo is very low and we do not show a CMD for this region, but its extension across a number of Magellan/Megacam pointings suggests that it is a real structure. A similar feature can be seen in the halo of M31, although the latter has a higher stellar density (SW Cloud, e.g., Bate et al. 2014). From its shape, it does not seem to be connected to any of the other substructures presented here.

5. DISCUSSION AND CONCLUSIONS

We have presented the widest-field RGB map to date of the extended halo of Cen A (Figs. 3 and 4), the closest elliptical galaxy. Our deep Magellan/Megacam imaging allows us to resolve old red giant branch populations out to a projected galactocentric radius of ~ 150 kpc, reaching very low surface brightness values ($\mu_{V,0} \sim 32$ mag arcsec $^{-2}$) and uncovering previously unknown tidally induced features and low-mass galaxies. In this contribution we described the most prominent of these features, including a disrupting satellite, pointing to the active interaction/accretion history for Cen A. We additionally introduced 13 newly discovered candidate satellites of which 9 are confirmed to be at the distance of Cen A (including the disrupting object), with absolute magnitudes in the range $M_V = -7.2$ to -13.0 , central surface brightness values of $\mu_{V,0} = 25.4 - 26.9$ mag arcsec $^{-2}$, and half-light radii of $r_h = 0.22 - 2.92$ kpc. The remaining 4 (unresolved) candidate satellites may be fainter than our detection limits ($M_V < -7$), or alternatively background unresolved galaxies. Two HST imaging programs (GO-13856 and GO-14259, PI: Crnojević) have already been approved to follow-up the newly discovered satellites (15 orbits) and the most prominent substructures in the halo of Cen A (20 orbits), respectively.

We can qualitatively compare the number and properties of the most prominent Cen A substructures to the ones found in M31 by PAndAS. A direct comparison is not straightforward due to the fact that the PAndAS survey reaches ~ 3.5 mag below the TRGB (e.g., Ibata et al. 2014), while PISCeS is limited to $\sim 1.5 - 2$ mag because of the larger distance of our target galaxy ($D \sim 3.8$ Mpc). Prior to PAndAS, the INT/WFC survey of the inner regions of M31 (Ferguson et al. 2002) led the charge with a combination of wide-field ground-based data and deep HST follow-up imaging (Ferguson et al. 2005; Richardson et al. 2008, 2009; Bernard et al. 2015). We seek to emulate this model with the current generation of wide-field imagers (e.g., Magellan/Megacam, Subaru/HyperSuprimeCam).

The PISCeS coverage of Cen A to date reveals two clear tidal streams, of which one still hosts an easily recognisable remnant (CenA-MM-Dw3), at least two shell-like features in the inner regions of the galaxy (Shell 1 and 2), and one diffuse “cloud” (Cloud S). The additional inhomogeneity in the central regions of Cen A is certainly due to accretion/interaction events, but caution should be used when analyzing this evidence in more detail, as the observing conditions for the pointings of interest vary greatly. As a first, crude comparison to the PAndAS discoveries, our Shell 1 and 2 resemble a scaled-up version of the NGC205 Loop or the NE Shelf (Ferguson et al. 2005). While our disrupting dwarf CenA-MM-Dw3 does

not have a counterpart in M31 (NGC147 is more luminous and its tails are fainter and less elongated; e.g., Crnojević et al. 2014a), the second stream uncovered by PISCeS is similar to Stream C or D to the South-East of M31 (e.g., Ibata et al. 2007; Lewis et al. 2013). As already mentioned, our Cloud S can be compared to the feature called the SW Cloud (Bate et al. 2014), even though the former is fainter and less spatially defined. The faintest feature in PAndAS is Stream A, at $\mu_{V,0} \sim 32$ mag arcsec $^{-2}$ (Ibata et al. 2007), while our faintest prominent feature (which we dub Dw3 NW) is located to the North-West of the stream of CenA-MM-Dw3, although it probably does not belong to the latter. We estimate Dw3 NW to have $\mu_{V,0} \sim 30.5$ mag arcsec $^{-2}$ based on the conversion from RGB number density to surface brightness of CenA-MM-Dw4 (see Fig. 10), i.e., the closest dwarf to Dw3 NW. The overall number of stream-like features in the halo of M31 seems to be higher than that found for Cen A, down to the PISCeS surface brightness limit, which is surprising given that the mass of Cen A is likely higher ($\sim 10^{12} M_\odot$ within the innermost 90 kpc, Woodley et al. 2007). However, simulations predict a large variety in the number of accretion and merger events experienced by a MW-mass halo, and our PISCeS Cen A map roughly compares to “Halo A” in Fig. 6 of Cooper et al. (2010), in terms of number of features above a surface brightness of $\mu_{V,0} \sim 30.5$ mag arcsec $^{-2}$.

Moving on to satellites, our discovery of 9 robust Cen A candidates from PISCeS can be compared to the M31 dwarfs discovered by the PAndAS survey. Once our survey is completed, by simply rescaling the number of discoveries to date to the final area we expect to find $\sim 6 \pm 2$ more satellites, which is fully consistent with the 14 dwarfs found in PAndAS over a similar projected area and within the same magnitude range ($-13 \lesssim M_V \lesssim -7$; see, e.g., Richardson et al. 2011). A more quantitative estimate of the faint end of the satellite luminosity function for Cen A will be presented once the full dataset is acquired.

Fig. 17 shows the global properties of the robust newly discovered satellites in the context of LG dwarfs (including CenA-MM-Dw1 and CenA-MM-Dw2 from Crnojević et al. 2014b). The two samples cover similar regions in the absolute magnitude vs central surface brightness and half-light radius vs absolute magnitude space. However, two of the PISCeS Cen A satellites have outlying properties in these distributions, i.e., they are very diffuse, with low surface brightness and large half-light radii for their absolute magnitude. Of these two objects, CenA-MM-Dw1 does not show any sign of distortion, while CenA-MM-Dw3 is clearly in an advanced tidal disruption phase. Despite this strong evidence, the possible location of CenA-MM-Dw3 behind Cen A and the uncertainty on its distance measurement imply that we cannot conclusively state that it is gravitationally bound to Cen A; our upcoming HST imaging will be crucial to definitively assess the distance of CenA-MM-Dw3. With its large extent and very low surface brightness, CenA-MM-Dw3 is one of the most extended and least dense objects known at its luminosity, together with another recent discovery of the PISCeS survey, i.e., the elongated Sculptor satellite Scl-MM-Dw2 (Toloba et al. 2016, but see also Romanowsky et al. 2016). These two satellites

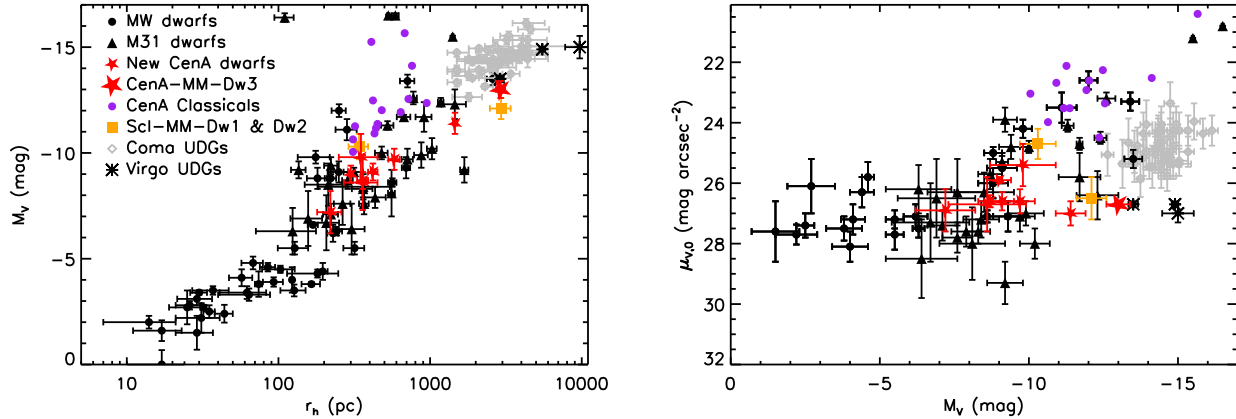


FIG. 17.— *Left panel*: Absolute V -band magnitude as a function of half-light radius for: MW/M31 dwarf galaxies (black points/triangles, from McConnachie 2012; Sand et al. 2012; Crnojević et al. 2014a; Drlica-Wagner et al. 2015; Kim et al. 2015; Kim & Jerjen 2015; Kopusov et al. 2015; Laevens et al. 2015a,b; Martin et al. 2015); previously known (“classical”) Cen A satellites (purple points, updated from Sharina et al. 2008); our newly discovered Cen A dwarfs (red stars); the remnant of the tidally disrupting CenA-MM-Dw3 (large red star); the newly discovered NGC 253 satellites found in PISCeS (yellow squares, Sand et al. 2014 and Toloba et al. 2016); and the new faint, diffuse galaxies found in Virgo and Coma by Mihos et al. (2015) and van Dokkum et al. (2015), respectively (black asterisks and grey diamonds). *Right panel*: Central V -band surface brightness as a function of absolute magnitude (symbols as before). The newly discovered Cen A companions have similar properties to those of LG dwarfs, except for the tidally disrupting CenA-MM-Dw3 which has a large half-light radius and low surface brightness for its absolute magnitude, similarly to Sagittarius in the Local Group, Scl-MM-Dw2 in Sculptor, and to the recently discovered diffuse Virgo galaxies. The new Cen A satellites have a consistently lower surface brightness than the “classical” Cen A satellites, and most of them have lower luminosity as well.

are comparable only to Sagittarius within the LG, however their properties can be compared to the recently discovered faint and diffuse galaxies in the Virgo and Coma clusters by Mihos et al. (2015) and van Dokkum et al. (2015), respectively. In particular, the two PISCeS objects have lower absolute magnitudes, but similar half-light radii and central surface brightness values to these unusual Virgo galaxies (see Fig. 17). The latter have been claimed to belong to a new class of extremely faint galaxies, and we clearly demonstrate that similar objects are also found in the Cen A and Sculptor groups. This result still holds even if we consider that the original (unperturbed) luminosity of CenA-MM-Dw3 might have been ~ 2 mag brighter than what we measured (see Sect. 4.2.3). CenA-MM-Dw3 is a heavily disrupting galaxy, and Scl-MM-Dw2 is likely ongoing a strong tidal interaction as well: this suggests that the Virgo and Coma diffuse galaxies might as well be experiencing disruption, but their tidal features, even if present, could not be detected within the surface brightness limits of these surveys ($\mu_{V,0} \sim 29 - 27$ mag arcsec $^{-2}$, respectively).

In the same plots, we also include the “classical” Cen A satellites. We choose to consider dwarfs for which resolved stellar studies are available from the literature, even though some of them have also structural parameters derived from integrated light (see, e.g., Jerjen et al. 2000). We include those dwarfs for which structural parameters have been derived by Sharina et al. (2008), and for which TRGB distance measurements are available from Karachentsev et al. (2007). There are a dozen additional “classical” Cen A satellites in the magnitude range $-15 \lesssim M_V \lesssim -10$ (see Karachentsev 2005; Karachentsev et al. 2007), but no structural parameter measurements are available in the literature for those. The original Sharina et al. (2008) distance moduli and extinction values are updated following Karachentsev et al. (2007) and the NASA Extragalactic

Database⁹, respectively. The new and previously known satellites are clearly distinct in their properties. While part of this is due to the different techniques used in deriving the parameters, the “classical” Cen A satellites certainly have a significantly higher central surface brightness/luminosity with respect to the new ones (see the right panel in Fig. 17). Interestingly, but perhaps unsurprisingly, all of the new objects, except for two, are fainter in absolute magnitude than the “classical” ones, demonstrating the effectiveness of PISCeS in extending the faint end of the satellite luminosity function for this elliptical galaxy. The newly discovered satellites bracket the previously known ones in terms of half-light radius, i.e., a few of them have smaller values and others much larger values. The two dwarfs with brighter magnitudes are very diffuse, which is likely why they were discovered by PISCeS and not previous work.

Finally, none of the newly discovered dwarfs are detected in neutral gas, as determined from the HI Parkes All Sky Survey (HIPASS; Barnes et al. 2001). We derive 5σ upper HI mass limits for our dwarfs and report them in Table 3. HIPASS is not sensitive enough to confirm or exclude the presence of HI in most of our targets, but we find an interesting upper limit of $M_{HI}/L_* \lesssim 0.4M_\odot/L_{\odot,B}$ for CenA-MM-Dw3. Our luminosity estimate for this object is a lower limit given its disrupting state, and thus the HI mass to light ratio is certainly even lower than the limit we derive, hinting at a genuine lack of gas for this dwarf. Previous HI studies of Cen A early-type satellites only find upper limits of $M_{HI} \lesssim 7 \times 10^3 M_\odot$ with $M_{HI}/L_B \lesssim 0.25M_\odot/L_{\odot,B}$ for this class of objects (Bouchard et al. 2007), suggesting that the environment of Cen A is very effective at removing gas reservoirs in these low-mass dwarfs (see also Crnojević et al. 2012).

We explore the possibility that the new PISCeS dwarfs

⁹ <http://ned.ipac.caltech.edu/>

belong to one of the Cen A planes of satellites recently described by Tully et al. (2015). In the cartesian Supergalactic coordinates plane (Tully et al. 2015, see the upper panel of their Fig. 1), these planes appear as thin, almost parallel distributions of satellites. Most of our new dwarfs seem to land on top of one of the planes: CenA-MM-Dw1/2/3/4/6 belong to Plane 1, CenA-MM-Dw7/8/9 are closer to Plane 2, while CenA-MM-Dw5 is found at an intermediate position between the two planes. Until velocities are obtained for the new satellites, the origin of these planes remains speculative.

In future contributions, we will further exploit this promising dataset in conjunction with our approved HST follow-up imaging, which will be completed in mid-2017. In particular, we will investigate the smooth versus discrete halo profile and stellar content of this elliptical (as done by the PAndAS and SPLASH surveys of M31, e.g., Ibata et al. 2014; Gilbert et al. 2012); the satellite luminosity function of Cen A as well as our observational detection limits (see, e.g., Chiboucas et al. 2013, for M81 satellites); the star formation histories and metallicities for the newly discovered dwarfs; and the star forming regions in the inner part of Cen A (e.g., Kraft et al. 2009; Neff et al. 2015a,b). The HST dataset will also put firmer constraints on the distances to the newly discovered satellites and halo features.

We conclude by underlining the crucial role played by our resolved PISCeS survey in characterizing the stellar populations of nearby galaxy halos, including tidal features and faint satellites, out to unprecedented galactocen-

tric distances. Surveys such as this represent a first step in the observational census of nearby galaxy halos and their inhabitants, allowing for the first time such investigations to be pushed beyond the limits of the LG and acting as prototype science cases for the next generation of ground-based and space-borne telescopes.

ACKNOWLEDGEMENTS

We are grateful to the referee for a careful reading of the manuscript and for his/her useful suggestions that helped improve this work. We warmly thank Maureen Conroy, John Roll, Sean Moran and David Osip for their prolonged efforts and help related to Megacam. DC wishes to kindly thank the hospitality of the Mullard Space Science Laboratory, University College of London, where part of this work has been carried out. DC, DJS, PG and ET acknowledge support from NSF grant AST-1412504; PG and ET acknowledge additional support from NSF grant AST-1010039; JDS acknowledges support from NSF grant AST-1412792. KS acknowledges support from the Natural Sciences and Engineering Research Council of Canada (NSERC). This work was supported in part by National Science Foundation Grant No. PHYS-1066293 and the Aspen Center for Physics. This paper uses data products produced by the OIR Telescope Data Center, supported by the Smithsonian Astrophysical Observatory. This research has made use of the NASA/IPAC Extragalactic Database (NED) which is operated by the Jet Propulsion Laboratory, California Institute of Technology, under contract with the National Aeronautics and Space Administration.

REFERENCES

- Amorisco, N. C. 2015, *MNRAS*, 450, 575
 Atkinson, A. M., Abraham, R. G., & Ferguson, A. M. N. 2013, *ApJ*, 765, 28
 Bailin, J., Bell, E. F., Chappell, S. N., Radburn-Smith, D. J., & de Jong, R. S. 2011, *ApJ*, 736, 24
 Barker, M. K., Ferguson, A. M. N., Irwin, M. J., Arimoto, N., & Jablonka, P. 2012, *MNRAS*, 419, 1489
 Barnes, D. G., Staveley-Smith, L., de Blok, W. J. G., et al. 2001, *MNRAS*, 322, 486
 Bate, N. F., Conn, A. R., McMonigal, B., et al. 2014, *MNRAS*, 437, 3362
 Bechtol, K., Drlica-Wagner, A., Balbinot, E., et al. 2015, *ApJ*, 807, 50
 Belokurov, V., & Koposov, S. E. 2016, *MNRAS*, 456, 602
 Belokurov, V., Zucker, D. B., Evans, N. W., et al. 2006, *ApJ*, 642, L137
 —. 2007, *ApJ*, 654, 897
 Bernard, E. J., Ferguson, A. M. N., Schlafly, E. F., et al. 2014, *MNRAS*, 443, L84
 Bernard, E. J., Ferguson, A. M. N., Richardson, J. C., et al. 2015, *MNRAS*, 446, 2789
 Bertin, E. 2010, *SWarp: Resampling and Co-adding FITS Images Together*, Astrophysics Source Code Library, ascl:1010.068
 Bonaca, A., Geha, M., & Kallivayalil, N. 2012, *ApJ*, 760, L6
 Bouchard, A., Jerjen, H., Da Costa, G. S., & Ott, J. 2007, *AJ*, 133, 261
 Boylan-Kolchin, M., Bullock, J. S., & Kaplinghat, M. 2011, *MNRAS*, 415, L40
 Bullock, J. S., & Johnston, K. V. 2005, *ApJ*, 635, 931
 Busha, M. T., Alvarez, M. A., Wechsler, R. H., Abel, T., & Strigari, L. E. 2010, *ApJ*, 710, 408
 Chiboucas, K., Jacobs, B. A., Tully, R. B., & Karachentsev, I. D. 2013, *AJ*, 146, 126
 Chiboucas, K., Karachentsev, I. D., & Tully, R. B. 2009, *AJ*, 137, 3009
 Cooper, A. P., Cole, S., Frenk, C. S., et al. 2010, *MNRAS*, 406, 744
 Côté, S., Draginda, A., Skillman, E. D., & Miller, B. W. 2009, *AJ*, 138, 1037
 Crnojević, D., Ferguson, A. M. N., Irwin, M. J., et al. 2013, *MNRAS*, 432, 832
 Crnojević, D., Grebel, E. K., & Cole, A. A. 2012, *A&A*, 541, A131
 Crnojević, D., Ferguson, A. M. N., Irwin, M. J., et al. 2014a, *MNRAS*, 445, 3862
 Crnojević, D., Sand, D. J., Caldwell, N., et al. 2014b, *ApJ*, 795, L35
 Da Costa, G. S., & Armandroff, T. E. 1990, *AJ*, 100, 162
 Dalcanton, J. J., Williams, B. F., Seth, A. C., et al. 2009, *ApJS*, 183, 67
 Deason, A. J., Belokurov, V., Evans, N. W., & Johnston, K. V. 2013, *ApJ*, 763, 113
 Dorman, C. E., Guhathakurta, P., Seth, A. C., et al. 2015, *ApJ*, 803, 24
 Dotter, A., Chaboyer, B., Jevremović, D., et al. 2008, *ApJS*, 178, 89
 Drlica-Wagner, A., Bechtol, K., Rykoff, E. S., et al. 2015, *ApJ*, 813, 109
 Duc, P.-A., Cuillandre, J.-C., Karabal, E., et al. 2015, *MNRAS*, 446, 120
 Ferguson, A. M. N., Irwin, M. J., Ibata, R. A., Lewis, G. F., & Tanvir, N. R. 2002, *AJ*, 124, 1452
 Ferguson, A. M. N., Johnson, R. A., Faria, D. C., et al. 2005, *ApJ*, 622, L109
 Gilbert, K. M., Guhathakurta, P., Beaton, R. L., et al. 2012, *ApJ*, 760, 76
 Greggio, L., Rejkuba, M., Gonzalez, O. A., et al. 2014, *A&A*, 562, A73
 Grillmair, C. J. 2006, *ApJ*, 645, L37
 —. 2009, *ApJ*, 693, 1118
 Grillmair, C. J., Cutri, R., Masci, F. J., et al. 2013, *ApJ*, 769, L23

- Guhathakurta, P., Ostheimer, J. C., Gilbert, K. M., et al. 2005, ArXiv Astrophysics e-prints, astro-ph/0502366
- Guhathakurta, P., Rich, R. M., Reitzel, D. B., et al. 2006, *AJ*, 131, 2497
- Harris, G. L. H., Rejkuba, M., & Harris, W. E. 2010, *PASA*, 27, 457
- Ibata, R., Martin, N. F., Irwin, M., et al. 2007, *ApJ*, 671, 1591
- Ibata, R. A., Gilmore, G., & Irwin, M. J. 1994, *Nature*, 370, 194
- Ibata, R. A., Lewis, G. F., McConnachie, A. W., et al. 2014, *ApJ*, 780, 128
- Israel, F. P. 1998, *A&A Rev.*, 8, 237
- Jacobs, B. A., Rizzi, L., Tully, R. B., et al. 2009, *AJ*, 138, 332
- Jerjen, H., Binggeli, B., & Freeman, K. C. 2000, *AJ*, 119, 593
- Jester, S., Schneider, D. P., Richards, G. T., et al. 2005, *AJ*, 130, 873
- Johnson, M. C., Kamphuis, P., Koribalski, B. S., et al. 2015, *MNRAS*, 451, 3192
- Johnston, K. V., Bullock, J. S., Sharma, S., et al. 2008, *ApJ*, 689, 936
- Karachentsev, I. D. 2005, *AJ*, 129, 178
- Karachentsev, I. D., Tully, R. B., Dolphin, A., et al. 2007, *AJ*, 133, 504
- Kim, D., & Jerjen, H. 2015, *ApJ*, 808, L39
- Kim, D., Jerjen, H., Mackey, D., Da Costa, G. S., & Milone, A. P. 2015, *ApJ*, 804, L44
- Koda, J., Yagi, M., Yamanoi, H., & Komiyama, Y. 2015, *ApJ*, 807, L2
- Koposov, S. E., Belokurov, V., Torrealba, G., & Evans, N. W. 2015, *ApJ*, 805, 130
- Koposov, S. E., Irwin, M., Belokurov, V., et al. 2014, *MNRAS*, 442, L85
- Kraft, R. P., Forman, W. R., Hardcastle, M. J., et al. 2009, *ApJ*, 698, 2036
- Laevens, B. P. M., Martin, N. F., Ibata, R. A., et al. 2015a, *ApJ*, 802, L18
- Laevens, B. P. M., Martin, N. F., Bernard, E. J., et al. 2015b, *ApJ*, 813, 44
- Lee, M. G., Freedman, W. L., & Madore, B. F. 1993, *ApJ*, 417, 553
- Lewis, G. F., Braun, R., McConnachie, A. W., et al. 2013, *ApJ*, 763, 4
- Lu, Z., Mo, H. J., Lu, Y., et al. 2015, *MNRAS*, 450, 1604
- Martin, N. F., Ibata, R. A., McConnachie, A. W., et al. 2013, *ApJ*, 776, 80
- Martin, N. F., Nidever, D. L., Besla, G., et al. 2015, *ApJ*, 804, L5
- Martínez-Delgado, D., Gabany, R. J., Crawford, K., et al. 2010, *AJ*, 140, 962
- McConnachie, A. W. 2012, *AJ*, 144, 4
- McConnachie, A. W., Irwin, M. J., Ibata, R. A., et al. 2009, *Nature*, 461, 66
- McLeod, B., Geary, J., Conroy, M., et al. 2015, *PASP*, 127, 366
- Merritt, A., van Dokkum, P., & Abraham, R. 2014, *ApJ*, 787, L37
- Mihos, J. C., Durrell, P. R., Ferrarese, L., et al. 2015, *ApJ*, 809, L21
- Monachesi, A., Bell, E. F., Radburn-Smith, D. J., et al. 2016, *MNRAS*, 457, 1419
- Moore, B., Ghigna, S., Governato, F., et al. 1999, *ApJ*, 524, L19
- Mouhcine, M., Ibata, R., & Rejkuba, M. 2010, *ApJ*, 714, L12
- Muñoz, R. P., Eigenthaler, P., Puzia, T. H., et al. 2015, *ApJ*, 813, L15
- Müller, O., Jerjen, H., & Binggeli, B. 2015, *A&A*, 583, A79
- Neff, S. G., Eilek, J. A., & Owen, F. N. 2015a, *ApJ*, 802, 88
- . 2015b, *ApJ*, 802, 87
- Okamoto, S., Arimoto, N., Ferguson, A. M. N., et al. 2015, *ApJ*, 809, L1
- Pearson, S., Küpper, A. H. W., Johnston, K. V., & Price-Whelan, A. M. 2015, *ApJ*, 799, 28
- Peng, E. W., Ford, H. C., Freeman, K. C., & White, R. L. 2002, *AJ*, 124, 3144
- Pillepich, A., Vogelsberger, M., Deason, A., et al. 2014, *MNRAS*, 444, 237
- Purcell, C. W., Bullock, J. S., & Zentner, A. R. 2007, *ApJ*, 666, 20
- Radburn-Smith, D. J., de Jong, R. S., Seth, A. C., et al. 2011, *ApJS*, 195, 18
- Rejkuba, M., Greggio, L., Harris, W. E., Harris, G. L. H., & Peng, E. W. 2005, *ApJ*, 631, 262
- Rejkuba, M., Harris, W. E., Greggio, L., et al. 2014, *ApJ*, 791, L2
- Richardson, J. C., Ferguson, A. M. N., Johnson, R. A., et al. 2008, *AJ*, 135, 1998
- Richardson, J. C., Ferguson, A. M. N., Mackey, A. D., et al. 2009, *MNRAS*, 396, 1842
- Richardson, J. C., Irwin, M. J., McConnachie, A. W., et al. 2011, *ApJ*, 732, 76
- Rizzi, L., Tully, R. B., Makarov, D., et al. 2007, *ApJ*, 661, 815
- Romanowsky, A. J., Martínez-Delgado, D., Martin, N. F., et al. 2016, *MNRAS*, 457, L103
- Salaris, M., Cassisi, S., & Weiss, A. 2002, *PASP*, 114, 375
- Sand, D. J., Spekkens, K., Crnojević, D., et al. 2015, *ApJ*, 812, L13
- Sand, D. J., Strader, J., Willman, B., et al. 2012, *ApJ*, 756, 79
- Sand, D. J., Crnojević, D., Strader, J., et al. 2014, *ApJ*, 793, L7
- Schlafly, E. F., & Finkbeiner, D. P. 2011, *ApJ*, 737, 103
- Schlegel, D. J., Finkbeiner, D. P., & Davis, M. 1998, *ApJ*, 500, 525
- Sharina, M. E., Karachentsev, I. D., Dolphin, A. E., et al. 2008, *MNRAS*, 384, 1544
- Stetson, P. B. 1987, *PASP*, 99, 191
- Stetson, P. B. 1993, in *IAU Colloq. 136: Stellar Photometry - Current Techniques and Future Developments*, ed. C. J. Butler & I. Elliott, 291
- . 1994, *PASP*, 106, 250
- Tissera, P. B., & Scannapieco, C. 2014, *MNRAS*, 445, L21
- Toloba, E., Sand, D. J., Spekkens, K., et al. 2016, *ApJ*, 816, L5
- Tully, R. B., Libeskind, N. I., Karachentsev, I. D., et al. 2015, *ApJ*, 802, L25
- van Dokkum, P. G., Abraham, R., Merritt, A., et al. 2015, *ApJ*, 798, L45
- Weinberg, D. H., Bullock, J. S., Governato, F., Kuzio de Naray, R., & Peter, A. H. G. 2013, ArXiv e-prints, arXiv:1306.0913
- Willman, B., Dalcanton, J. J., Martínez-Delgado, D., et al. 2005, *ApJ*, 626, L85
- Woodley, K. A., Harris, W. E., Beasley, M. A., et al. 2007, *AJ*, 134, 494